



## A three-invariant cap-plasticity damage model for cementitious materials



B. Paliwal<sup>a,\*</sup>, Y. Hammi<sup>a</sup>, R.D. Moser<sup>b</sup>, M.F. Horstemeyer<sup>a</sup>

<sup>a</sup>Center for Advanced Vehicular Systems, 200 Research Blvd., Starkville, MS 39759, USA

<sup>a</sup>Department of Mechanical Engineering, Box-9552 Carpenter Building, Mississippi State University, MS 39762, USA

<sup>b</sup>Geotechnical and Structures Laboratory, US Army Engineer Research & Development Center, Vicksburg, MS 39180, USA

### ARTICLE INFO

#### Article history:

Received 9 March 2016

Revised 3 November 2016

Available online 21 December 2016

#### Keywords:

Cement

Concrete

Cap-plasticity

Damage mechanics

Constitutive model

Multi-axial loading

### ABSTRACT

We present a new continuum elastoplastic damage model for cementitious materials which captures their distinct behavior in tension and compression due to crack-induced damage and irreversible plastic deformation. It also describes their response under multi-axial loading with low to high confining pressures. A smooth, closed-convex three stress-invariant yield surface is developed which perpendicularly intersects the negative hydrostatic axis and is composed of a shear loading surface and an elliptical cap. It incorporates a plastic internal state variable (ISV) characterizing non-uniform hardening of both shear loading surface and elliptical cap, while the flow rule is considered to have volumetric non-associativity. Damage evolution laws incorporate two ISVs describing crack growth at the macroscale under tensile and compressive stresses separately. Overall damage under multiaxial loading explicitly considers the effect of confining stresses on damage evolution and stiffness recovery effects under cyclic loading. Model predictions are compared against several experimental results on various concretes and also against responses of recently reported models. The proposed model predicts distinctive features of concrete very well including hardening behavior in triaxial-compression and both pre- and post-peak volumetric behavior.

© 2016 Elsevier Ltd. All rights reserved.

### 1. Introduction

Throughout many years, several theoretical and computational models involving continuum plasticity and/or damage mechanics have been developed to simulate the mechanical behavior of cementitious materials like concrete, *c.f.* (Caner and Bazant, 2013; Etse and Willam, 1994; Folino and Etse, 2012; Grassl et al., 2013; Han and Chen, 1987; Lee and Fenves, 1998; Lubliner et al., 1989; Luccioni et al., 1996; Papanikolaou and Kappos, 2007; Salari et al., 2004; Sánchez et al., 2011; Voyiadjis et al., 2008; Wu et al., 2006). Concrete is the most widely used construction material in the world; however, appropriate modeling of its experimentally observed behavior under multi-axial loading conditions, particularly under confined compression, is still challenging. There are many experimental studies showing that depending on the stress state and more specifically on the confinement level, failure modes in concrete change drastically, *c.f.* (Burlion et al., 2001; Imran and Pantazopoulou, 1996; Lu et al., 2007; Poinard et al., 2010; Sfer et al., 2002) among many others.

Under predominantly tensile loading with zero to low confinement, concrete experiences nucleation, rapid growth, and coalescence of micro-cracks, forming highly localized fracture zones, accompanied by strain softening and significant degradation of elastic stiffness. Its response under tension is much more brittle displaying considerably lower strength levels and negligible plastic hardening compared with its response under compressive loading states. At the other end of the spectrum, under triaxial compression with high confining stresses, concrete is remarkably ductile displaying considerable plastic deformation with limited micro-cracking. The stiffness degradation is very limited as well with no well-defined peak stress – the axial stress vs. strain curve shows a hardening response characterized by a monotonically decreasing slope tending toward a plateau – and inelastic volumetric dilatancy is also greatly reduced, *c.f.* (Poinard et al., 2010; Sfer et al., 2002). Under massive confining stresses, an additional inelastic mechanism characterized by material densification (or compaction) due to collapse of micro-porous constituents and micro-voids is also activated, particularly in mortar in the vicinity of mortar-aggregate interface, *c.f.* (Bažant et al., 1986; Burlion et al., 2001). On the other hand, under moderate confining pressures, concrete exhibits both ductility – characterized by irreversible plastic deformation which strongly increases with confinement – and micro-cracking,

\* Corresponding author.

E-mail address: [bp983@msstate.edu](mailto:bp983@msstate.edu) (B. Paliwal).

microcrack sliding and material crushing – which results in noticeable inelastic volumetric expansion and material stiffness degradation, *c.f.* (Poinard et al., 2010).

Therefore, in order to appropriately address the full spectrum of concrete inelastic deformation and failure modes – both, due to plasticity and micro-cracking under multiaxial loading subjected to various levels of confinement – and, furthermore, accounting for the continuous transition from brittle to ductile failure behavior, an elastoplastic-damage model which is based on both, irreversible plastic deformation and continuum damage mechanics, is required.

Many authors have developed constitutive models which combine flow theory of plasticity with damage while describing the mechanical behavior of concrete and rock-like geological materials, *c.f.* (Cicekli et al., 2007; Lee and Fenves, 1998; Lubliner et al., 1989; Luccioni et al., 1996; Salari et al., 2004; Voyiadjis et al., 2008; Wu et al., 2006). Almost all of these models seem capable to describe the plastic-shear deformation and crack-induced damage evolution under low to moderate confinement. They, however, are not suitable to describe the related inelastic deformation under high confinement range including pore collapse hardening processes under massive confinement. For example, under hydrostatic compressive loading, concrete first exhibits somewhat softening behavior beyond its elastic limit under low pressure. As the pressure increases an increasing stiffening behavior is observed because of material densification *i.e.* concrete exhibits a small reversible (or elastic) regime followed by an elastoplastic regime where both the tangent moduli and bulk secant moduli increase as the result of compaction (Burlion et al., 2001). Such non-linear behavior cannot be predicted using aforementioned models.

On the other hand, up until recently, several models specifically for concrete are developed which are also based on flow theory of plasticity and potentially can describe some of its inelastic deformation behavior under high-confinement, *c.f.* (Etse and Willam, 1994; Folino and Etse, 2012; Grassl et al., 2013). In these models, hardening in pre-peak regime is described using ‘closed’ (or bounded) evolving yield surfaces which intersects both positive and negative side of hydrostatic pressure axis. Although, post-peak softening behavior is described using fracture energy concepts ( ), they, however, are unable to capture some of its crucial behaviors including either crack-induced stiffness degradation, or stiffness recovery during cyclic loading, particularly as loading changes from being predominantly tensile to predominantly compressive furthering crack-closure effects. Moreover, even though models *e.g.* Grassl et al. (2013) use single plastic yield surface and account for the damage, transition across the negative hydrostatic axis is not smooth as they do not intersect it perpendicularly.

Considering all of the above, in this work we present a continuum elastoplastic damage model for concrete which captures its distinct behavior in tension and compression both, due to crack-induced damage and irreversible plastic deformation, while also describing its response under multi-axial loading with low to high confining pressures. Irreversible deformation is described using flow theory of plasticity which is considered to operate in the effective configuration pertaining to the undamaged material. The yield surface is composed of a shear loading surface and an elliptical cap; it is smooth, and is perpendicular to the negative hydrostatic axis.

The evolution law of plastic internal state variable (ISV) characterizes the non-uniform isotropic hardening behavior in which both shear loading surface and elliptical cap undergo hardening. The flow rule is considered to have volumetric non-associativity as it has been reported that associative flow rule over estimate the volumetric dilatancy (Etse and Willam, 1994; Smith et al., 1989).

Next, we have adopted the hypothesis of strain equivalence to incorporate the effects of damage (Lämmer and Tsakmakis, 2000; Ju, 1990; Lemaitre, 1985; Lemaitre and Chaboche, 1998; Menzela et al., 2005; Voyiadjis and Taqieddin, 2009). It is noted that in ductile, quasi-brittle, and brittle materials, the damage evolution, as a function of deformation, is typically divided into three components – void/crack nucleation, growth, and coalescence (*c.f.* (Garrison and Moody, 1987), (Horstemeyer et al., 2000), (Paliwal and Ramesh, 2008)). In the present framework, separate rules characterizing crack nucleation, growth and coalescence are not specified. Instead, the underlying micromechanical processes of crack nucleation, growth and coalescence are represented as coupled and approximated at the macro-continuum scale with the help of a damage evolution law which incorporates appropriate damage ISVs. Two damage ISVs describing tensile and compressive damage evolution separately are introduced. An isotropic scalar damage parameter characterizing overall damage under multiaxial loading is subsequently formulated which explicitly considers both, the stiffness recovery effects under cyclic loading and the effect of confining stresses on damage evolution under predominantly compressive loading.

The paper is structured as follows – in the next section and its subsections, we describe the framework for the elastoplastic-damage model followed by the description of individual components and features constituting both plasticity and damage. Section 3 describes the procedure pertaining to calibration of model parameters using conventional tensile and unconfined and confined compression tests. This is followed by Section 4 which presents the comparisons between the model response and experimental data under wide range of loading scenarios including compression under both low and high confinement. Finally, Section 5 summarizes the work.

## 2. Elastoplastic – damage model

### 2.1. Framework

This section describes a framework of three dimensional damage-plasticity model developed for concrete. Damage at the macroscopic scale due to growth and coalescence of micro-cracks is described by the isotropic damage parameter  $D$  where  $D \in [0, 1]$ ; value  $D=0$  and  $D=1$  correspond to undamaged virgin state and complete ruptured state, respectively. It is a function of two parameters – tensile damage  $D^+$ , and compressive damage  $D^-$  – characterizing the degradation of mechanical properties of concrete under tension and compression, respectively. Using Lemaitre’s strain equivalence hypothesis (Lemaitre, 1985), homogenized stress  $\sigma_{ij}$  associated with the damaged state, is mapped onto the stress  $\bar{\sigma}_{ij}$  in the effective undamaged state as follows

$$\bar{\sigma}_{ij} = \frac{\sigma_{ij}}{(1-D)} \quad (1)$$

The bar on the top of the variable means that it is expressed in the effective (undamaged) space. Next, we use the following coupling relationship for damage parameter  $D$  which couples both tensile and compressive damage parameters as well as a function defining elastic stiffness recovery during transition from tensile to compressive loading, as described by Lee and Fenves (1998)

$$D = 1 - (1 - s(\bar{\sigma}_{ij})D^+)(1 - D^-) \quad (2)$$

where  $s(\bar{\sigma}_{ij})$  which is a function of stress state such that  $s(\bar{\sigma}_{ij}) \in [0, 1]$ , is defined as follows

$$s(\bar{\sigma}_{ij}) = s_0 + (1 - s_0)R(\bar{\sigma}_{ij}) \quad (3)$$

Here,  $s_0 \in [0, 1]$  is a constant, and dimensionless parameter  $R(\bar{\sigma}_{ij}) \in [0, 1]$  is a weight factor (c.f. Lubliner et al., 1989) defined as follows

$$R(\bar{\sigma}_{ij}) = \begin{cases} 0 & \bar{\sigma}_{ij} = 0 \\ \frac{\sum_{k=1}^3 \langle \bar{\sigma}_k \rangle}{\sum_{k=1}^3 |\bar{\sigma}_k|} & \text{otherwise} \end{cases} \quad (4)$$

where,  $\langle x \rangle = \frac{1}{2}(|x| + x)$  denotes the Macauley bracket function, and  $\bar{\sigma}_k$ ,  $k = 1, 2, 3$  are principal stress values of  $\bar{\sigma}_{ij}$ . Note that any value of  $s$  between 0 and 1 results in a partial recovery of elastic stiffness during the transition from tensile to compressive loading. If all principal stresses are positive,  $s=R=1$  and  $D=1-(1-D^+)(1-D^-)$  which implies no stiffness recovery during the transition from compression to tension. On the other hand, if all principal stresses are negative,  $s=s_0$ ;  $R=0$  and  $D=1-(1-s_0 D^+)(1-D^-)$  which implies full elastic stiffness recovery if  $s_0=0$ , and no recovery if  $s_0=1$ .

Next, we can decompose the strain tensor  $\varepsilon_{ij}$  into its elastic,  $\varepsilon_{ij}^e$ , and plastic part,  $\varepsilon_{ij}^p$ , and the following can be expressed from linear elasticity

$$\varepsilon_{ij} = \varepsilon_{ij}^e + \varepsilon_{ij}^p; \quad \sigma_{ij} = E_{ijkl}(\varepsilon_{kl} - \varepsilon_{kl}^p) \quad (5)$$

where  $E_{ijkl}$  is the elastic stiffness tensor of the damaged material. From Eqs. (1) and (5<sub>2</sub>), we subsequently obtain

$$\bar{\sigma}_{ij} = \frac{E_{ijkl}}{(1-D)}(\varepsilon_{kl} - \varepsilon_{kl}^p) = E_{ijkl}^0(\varepsilon_{kl} - \varepsilon_{kl}^p) \quad (6)$$

where  $E_{ijkl}^0$  is the elastic stiffness tensor of the virgin material. Eq. (6) also suggest that the effective stress is defined with respect to undamaged state and the overall damage parameter  $D$  represents the degradation of the elastic stiffness. In what follows, the characterization of the plastic response is formulated in the effective stress space where  $\bar{\sigma}_{ij}$  is determined from the evolution law for the plastic strain  $\varepsilon_{ij}^p$  expressed as follows (repeated indices imply summation)

$$\dot{\varepsilon}_{ij}^p = \dot{\lambda} \frac{\partial F^p(\bar{\sigma}_{ij}, \kappa^p)}{\partial \bar{\sigma}_{ij}} = \dot{\lambda} m_{ij} \quad (\text{flow rule})$$

$$\dot{\kappa}^p = \dot{\lambda} h^p(\bar{\sigma}_{ij}, \kappa^p) \quad (\text{hardening law})$$

$$F(\bar{\sigma}_{ij}, \kappa^p) \leq 0; \quad \dot{\lambda} \geq 0; \quad \dot{\lambda} F = 0 \quad (\text{loading - unloading})$$

Kuhn - Tucker complementary conditions)

$$\dot{\lambda} \dot{F}(\bar{\sigma}_{ij}, \kappa^p) = \dot{\lambda} \left( \frac{\partial F}{\partial \bar{\sigma}_{ij}} \dot{\bar{\sigma}}_{ij} + \frac{\partial F}{\partial \kappa^p} \dot{\kappa}^p \right) = 0 \quad (\text{consistency condition}) \quad (7)$$

In Eq. (7),  $\dot{\lambda}$  is the plastic multiplier,  $F^p$  is the plastic potential, and function  $F$  represents the yield surface which determines the admissible stress states.  $F$  is not the same as plastic potential function  $F^p$  if the flow rule is non-associative, implying that the direction of the plastic strain rate vector is normal to the plastic potential surface ( $F^p=0$ ) which is different from the vector normal to the yield surface ( $F=0$ ).  $\kappa^p$  is the ISV characterizing isotropic hardening, evolution of which is determined using a plastic hardening function  $h^p$ .

Damage parameters  $D^+$  and  $D^-$  are functions of tensile and compressive ISVs  $\kappa^+$  and  $\kappa^-$ , respectively. Damage loading function and evolution laws of ISVs along with damage loading/unloading conditions according to Kuhn-Tucker relations are given as follows

$$F_D^\pm = F^\pm - \kappa^\pm; \quad F^\pm = \int_0^t \dot{F}^\pm(R(\bar{\sigma}_{ij}), \dot{\varepsilon}^{p\pm}) dt \quad (8)$$

$$F_D^\pm \leq 0; \quad \dot{\kappa}^\pm \geq 0; \quad \dot{\kappa}^\pm F_D^\pm = 0$$

where,  $t$  represents time,  $F_D^\pm$  are the damage loading functions, and functions  $\dot{F}^\pm$  depend on parameter  $R(\bar{\sigma}_{ij})$  (see Eq. (4)) and on equivalent plastic strain rates  $\dot{\varepsilon}^{p\pm}$  (see Eq. 34 and Eqs. (46, 47) later in Section 2.3.3 for the definitions of  $\dot{F}^+$ ,  $\dot{\varepsilon}^{p+}$  and  $\dot{F}^-$ ,  $\dot{\varepsilon}^{p-}$ , respectively). Corresponding damage consistency conditions during damage evolution can be obtained as follows

$$F_D^\pm = \dot{F}_D^\pm = 0 \Rightarrow F^\pm = \kappa^\pm; \quad \dot{F}^\pm = \dot{\kappa}^\pm \geq 0 \quad (9)$$

Using relationships presented in Eqs. (7) and (8), we can obtain continuum elastoplastic-damage tangent modulus as follows. During plastic loading, we have from consistency condition (Eq. (7<sub>4</sub>))

$$\frac{\partial F}{\partial \bar{\sigma}_{ij}} \dot{\bar{\sigma}}_{ij} + \frac{\partial F}{\partial \kappa^p} \dot{\kappa}^p = \frac{\partial F}{\partial \bar{\sigma}_{ij}} E_{ijkl}^0 (\dot{\varepsilon}_{kl} - \dot{\varepsilon}_{kl}^p) + \frac{\partial F}{\partial \kappa^p} \dot{\lambda} h^p = 0 \quad (10)$$

using the flow rule from Eq. (7<sub>1</sub>) in Eq. (10), we can solve for the consistency parameter as follows

$$\dot{\lambda} = \frac{\frac{\partial F}{\partial \bar{\sigma}_{ij}} E_{ijkl}^0 \dot{\varepsilon}_{kl}}{\frac{\partial F}{\partial \bar{\sigma}_{ij}} E_{ijkl}^0 \frac{\partial F^p}{\partial \bar{\sigma}_{kl}} - \frac{\partial F}{\partial \kappa^p} h^p} = \frac{1}{\psi} \frac{\partial F}{\partial \bar{\sigma}_{ij}} E_{ijkl}^0 \dot{\varepsilon}_{kl} \quad (11)$$

substituting Eq. (11) into Eqs. (7<sub>1</sub>) and (5) we can obtain effective elastoplastic tangent modulus  $\bar{C}_{ijkl}^{ep}$  as follows

$$\dot{\bar{\sigma}}_{ij} = \left[ E_{ijkl}^0 - \frac{1}{\psi} \left( E_{ijmn}^0 \frac{\partial F^p}{\partial \bar{\sigma}_{mn}} \right) \left( E_{pqkl}^0 \frac{\partial F}{\partial \bar{\sigma}_{pq}} \right) \right] \dot{\varepsilon}_{kl} = \bar{C}_{ijkl}^{ep} \dot{\varepsilon}_{kl} \quad (12)$$

Derivation of elastoplastic-damage tangent modulus  $\bar{C}_{ijkl}^{ep}$ , which is obtained after time-differentiating Eq. (1<sub>1</sub>) is given in Appendix A

## 2.2. Plasticity model

The plasticity model developed in this work includes a yield criteria using pressure and Lode angle sensitive yield function, a non-associative plastic flow rule, a hardening law accompanied by an evolution law of the ISV used in the hardening law. The yield function and the plastic potential are formulated in the Haigh-Westergaard coordinate system which is defined by the cylindrical coordinates  $\xi$ ,  $\bar{\rho}$  and  $\bar{\theta}$  representing the hydrostatic component, the deviatoric component and the Lode angle component, respectively. These coordinates are functions of the invariants  $\bar{I}_1$ ,  $\bar{J}_2$  and  $\bar{J}_3$  expressed in terms of the principal stress tensors  $\bar{\sigma}_1$ ,  $\bar{\sigma}_2$  and  $\bar{\sigma}_3$  (where  $\bar{\sigma}_1 > \bar{\sigma}_2 > \bar{\sigma}_3$ ) as follows

$$\xi = \frac{\bar{I}_1}{\sqrt{3}}; \quad \bar{I}_1 = \bar{\sigma}_1 + \bar{\sigma}_2 + \bar{\sigma}_3$$

$$\bar{\rho} = \sqrt{2\bar{J}_2}; \quad \bar{J}_2 = \frac{1}{6} [(\bar{\sigma}_1 - \bar{\sigma}_2)^2 + (\bar{\sigma}_2 - \bar{\sigma}_3)^2 + (\bar{\sigma}_3 - \bar{\sigma}_1)^2]$$

$$\bar{\theta} = \frac{1}{3} \cos^{-1} \left( \frac{3\sqrt{3}}{2} \frac{\bar{J}_3}{\bar{J}_2^{3/2}} \right); \quad \bar{J}_3 = \left( \bar{\sigma}_1 - \frac{\bar{I}_1}{3} \right) \left( \bar{\sigma}_2 - \frac{\bar{I}_1}{3} \right) \left( \bar{\sigma}_3 - \frac{\bar{I}_1}{3} \right) \quad (13)$$

### 2.2.1. Yield surface

In this work, we have developed a smooth yield-surface which perpendicularly intersects the negative hydrostatic axis. For this yield function at any hardening level, all points in the principal stress space such that  $F \leq 0$ , constitute a closed-convex set. This set is also bounded for  $q < 1$  because of the elliptical cap  $F_C$  ( $F_C$  is described later in the section). In the past, several studies characterizing mechanical behavior of concrete have used open yield surface while describing the evolution of plastic strain (c.f. (Cervenka and Papanikolaou, 2008; Grassl et al., 2002; Papanikolaou and Kappos, 2007; Sánchez et al., 2011)). As a result, these models fail to account for plastic deformation under high pressure loading conditions there is no limit to the elastic zone on the negative

part of the pressure axis. This is in contrast with some of the reported experimental evidence which suggest plastic flow under pure hydrostatic loading (c.f. (Bažant et al., 1996; Green and Swanson, 1973; Sfer et al., 2002)). On the other hand, there are studies which consider bounded yield surface; some of them, however, are represented by either  $C^0$  continuous curves (c.f. (Han and Chen, 1987)) or higher order  $C^1$  continuous curves which does not intersect the negative pressure axis perpendicularly (c.f. (Etse and Willam, 1994)). The function describing the yield surface developed in this work does not have these limitations. It has two main components – a shear loading function  $F_L$  (defines the ‘cone’ region), and an elliptical cap function  $F_C$  (used to define the ‘cap’ region). The shear loading function is a pressure and Lode angle sensitive three parameter function similar to the one proposed by Menétrey and Willam (1995). The three parameters required are uniaxial compressive strength  $f_c$ , uniaxial tensile strength  $f_t$  and equibiaxial compressive strength  $f_b$ . Subsequently, function  $F_L$  is given in terms of effective stress (in Haigh–Westergaard coordinate) as follows

$$F_L(\bar{\xi}, \bar{\rho}, \bar{\theta}, q(\kappa^p)) \equiv \left( \sqrt{\frac{3}{2}} \frac{\bar{\rho}}{f_c} \right)^2 + m_0 q^2 (\kappa^p) \times \left( \frac{\bar{\rho}}{\sqrt{6} f_c} \Gamma(\cos \bar{\theta}, e) + \frac{\bar{\xi}}{\sqrt{3} f_c} \right) - q^2 (\kappa^p) = 0 \quad (14)$$

The shape of meridians of  $F_L$  on the Rendulic plane ( $\bar{\rho} - \bar{\xi}$  plane) is parabolic, and on the deviatoric plane (plane  $\bar{\xi} = \text{constant}$ ) it varies from triangular to almost circular with increasing confinement. Elliptic function  $\Gamma(\cos \bar{\theta}, e)$  proposed by Willam and Warnke (1975) is used here which controls the shape of the deviatoric section, given as

$$\Gamma(\cos \bar{\theta}, e) = \frac{4(1 - e^2) \cos^2 \bar{\theta} + (2e - 1)^2}{2(1 - e^2) \cos \bar{\theta} + (2e - 1) \sqrt{4(1 - e^2) \cos^2 \bar{\theta} + 5e^2 - 4e}} \quad (15)$$

The eccentricity parameter  $e$  is evaluated from the three parameters using the relationship proposed by Jirásek and Bažant (2002, pp. 365) as follows

$$e = \frac{1 + \epsilon}{2 - \epsilon}, \quad \text{where } \epsilon = \frac{f_t}{f_b} \left( \frac{f_b^2 - f_c^2}{f_c^2 - f_t^2} \right) \quad (16)$$

Finally, friction parameter  $m_0$  is given as

$$m_0 = 3 \frac{f_c^2 - f_t^2}{f_c f_t} \frac{e}{e + 1} \quad (17)$$

The evolution of the loading surface during hardening is controlled by a hardening function  $q(\kappa^p)$ , which depends on an isotropic ISV  $\kappa^p$ , and is described in detail in the next section. Fig. 1 shows the plots of the loading function on the Rendulic plane for various  $q(\kappa^p)$ . The maximum value  $q(\kappa^p)$  is equal to one (corresponding to  $\kappa^p = 1$  as described in later section) at which the loading surface becomes the failure surface as proposed by Menétrey and Willam (1995)

$$F(\bar{\xi}, \bar{\rho}, \bar{\theta}, 1) \equiv F_L(\bar{\xi}, \bar{\rho}, \bar{\theta}, 1) \equiv \frac{3}{2} \left( \frac{\bar{\rho}}{f_c} \right)^2 + m_0 \left( \frac{\bar{\rho}}{\sqrt{6} f_c} \Gamma(\cos \bar{\theta}, e) + \frac{\bar{\xi}}{\sqrt{3} f_c} \right) - 1 = 0 \quad (18)$$

Note that  $\Gamma(\cos \bar{\theta}, e) = 1$  and  $1/e$  for compressive and tensile meridian, respectively. Parameters  $e$  and  $m_0$  are obtained in terms of  $f_c$ ,  $f_t$  and  $f_b$  (Eqs. (16), (17)) by substituting corresponding values of  $\bar{\rho}$  and  $\bar{\xi}$  in Eq. (18) at peak stress levels, for cases of uniaxial tensile and equibiaxial compressive loading ( $\Gamma(\cos \bar{\theta}, e) = 1/e$

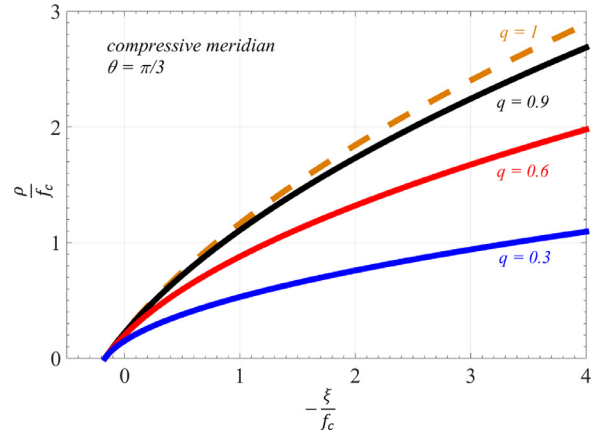


Fig. 1. Evolution of the compressive meridian of the shear loading function  $F_L$  in Rendulic plane during hardening.

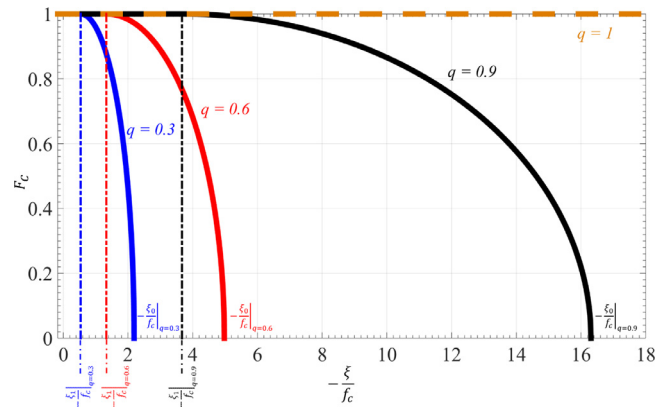


Fig. 2. Plots of the cap function  $F_C$  vs.  $-\frac{\xi}{f_c}$  for different levels of hardening.

for both cases). This results in two bilinear equations which are solved simultaneously to obtain expressions for  $e$  and  $m_0$  as given in Eqs. (16), (17).

The second component of the yield function is the elliptical cap function  $F_C$  which determines at what point the yield surface intersects  $\bar{\xi} -$  axis in compression. This intersection point corresponds to  $(\bar{\xi}_0, 0) \equiv (\bar{\xi}_0(q(\kappa_1^p)), 0)$  which is also where the plastic deformation commences in pure hydrostatic loading for a given level of hardening  $\kappa_1^p$ . Further loading leads to the evolution of hardening to  $\kappa_2^p$  which also changes the intersection point to  $(\bar{\xi}_0(q(\kappa_2^p)), 0)$ . The cap function used in this study is described as follows

$$F_C(\bar{\xi}, q(\kappa^p)) = \begin{cases} 1 & \text{if } \bar{\xi} > \bar{\xi}_1(q(\kappa^p)) \\ \sqrt{1 - \left( \frac{\bar{\xi} - \bar{\xi}_1(q(\kappa^p))}{\bar{\xi}_0(q(\kappa^p)) - \bar{\xi}_1(q(\kappa^p))} \right)^2} & \text{if } \bar{\xi} \leq \bar{\xi}_1(q(\kappa^p)) \end{cases} \quad (19)$$

The intersection point  $(\bar{\xi}_0, 0)$  is, therefore, a function of  $\kappa^p$ . Similarly, the transition point  $(\bar{\xi}_1, 1) \equiv (\bar{\xi}_1(q(\kappa^p)), 1)$  is also a function of  $q(\kappa^p)$ ; once the ISV  $\kappa^p$  is known, both  $\bar{\xi}_0$  and  $\bar{\xi}_1$  can be evaluated. Fig. 2 shows plots of the cap function on the Rendulic plane for various  $q(\kappa^p)$ . Finally, the yield surface  $F$  is obtained using  $F_L$  and  $F_C$  as follows

$$F(\bar{\xi}, \bar{\rho}, \bar{\theta}, q(\kappa^p)) \equiv \left[ \sqrt{\frac{3}{2}} \frac{\bar{\rho}}{f_c} \right]^2 + q^2(\kappa^p) \left[ m_0 \frac{\bar{\rho}}{\sqrt{6} f_c} \Gamma(\cos \bar{\theta}) + \left( m_0 \frac{\bar{\xi}}{\sqrt{3} f_c} - 1 \right) \left( F_C(\bar{\xi}, q(\kappa^p)) \right)^2 \right] = 0 \quad (20)$$

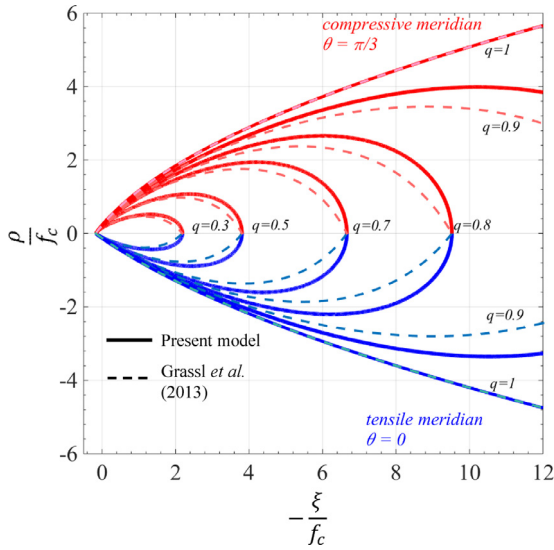


**Fig. 3.** Evolution of the compressive and tensile meridians of the yield surface  $F$  in Rendulic plane during hardening. Results from present model are compared with results from [Grassl et al. \(2013\)](#).

The transition point  $(\bar{\xi}_1, 1)$  on the cap surface  $F_C$  corresponds to the transition point  $(\bar{\xi}_1, \bar{\rho}_1)$  on the yield surface  $F$ . Note that for  $\bar{\xi} > \bar{\xi}_1$ , the yield surface  $F$  is identical to the shear loading surface  $F_L$  defined in [Eq. \(17\)](#) as  $F_C = 1$  for  $\bar{\xi} > \bar{\xi}_1$ . Both  $\bar{\xi}_0$  and  $\bar{\xi}_1$  are determined as a function of  $q(\kappa^p)$  by using the yield surface of extended Leon model ([Etse and Willam, 1994](#)) modified by [Grassl and Jirásek \(2006\)](#) denoted as  $F^{GJ}$  which is given by the following equation,

$$F^{GJ}(\bar{\xi}, \bar{\rho}, \bar{\theta}, q(\kappa^p)) \equiv \left( (1 - q(\kappa^p)) \left( \frac{\bar{\rho}}{\sqrt{6}f_c} + \frac{\bar{\xi}}{\sqrt{3}f_c} \right)^2 + \sqrt{\frac{3}{2}} \frac{\bar{\rho}}{f_c} \right)^2 + m_0 q^2(\kappa^p) \left( \frac{\bar{\rho}}{\sqrt{6}f_c} \Gamma(\cos \bar{\theta}) + \frac{\bar{\xi}}{\sqrt{3}f_c} \right) - q^2(\kappa^p) = 0 \quad (21)$$

This yield surface also becomes the failure surface proposed by [Menétrey and Willam \(1995\)](#) as described in [Eq. \(18\)](#) for  $q(\kappa^p) = 1$ . The intersection point  $(\bar{\xi}_0, 0)$  as a function of hardening  $q(\kappa^p)$  is determined by substituting it in [Eq. \(21\)](#) and solving the resulting quartic equation. The detailed steps are described in [Appendix B.1](#). Furthermore, the transition point at  $(\bar{\xi}_1, \bar{\rho}_1)$  is determined by computing first the stress coordinate  $(\bar{\xi}_{max}, \bar{\rho}_{max})$  which is the maxima of the yield surface  $F^{GJ}$  described in [Eq. \(21\)](#). The ordinate  $\bar{\rho}_1(q(\kappa^p))$  of the transition point (which is less than  $\bar{\rho}_{max}$ ) is given as,

$$\bar{\rho}_1 = \alpha \bar{\rho}_{max}; \quad 0 < \alpha < 1 \quad (22)$$

Once  $\bar{\rho}_1$  is known, the abscissa  $\bar{\xi}_1$  can be determined by substituting it in [Eq. \(20\)](#) (note that where  $F_C = 1$  at the transition point) and is evaluated as follows,

$$\bar{\xi}_1(q(\kappa^p)) = \frac{f_c \sqrt{3}}{m_0(q(\kappa^p))^2} \times \left( q^2(\kappa^p) - \frac{m_0 q^2(\kappa^p) \Gamma(\cos \bar{\theta})}{\sqrt{6}} \frac{\bar{\rho}_1}{f_c} - \frac{3}{2} \left( \frac{\bar{\rho}_1}{f_c} \right)^2 \right) \quad (23)$$

The detailed calculations are presented in [Appendix B.2](#).

[Fig. 3](#) shows the evolution of the resulting tensile and compressive meridian plots of the yield surface  $F$  alongside  $F^{GJ}$  during hardening in the Rendulic plane. Finally, [Fig. 4](#) shows the three-dimensional representation of  $F$  in principal stress space with traces of several meridians and deviatoric-plane cross-sections.

### 2.2.2. Hardening law

The positioning and the shape of the yield surface is controlled by a scalar non-dimensional hardening parameter  $q(\kappa^p)$  which is a function of hardening ISV  $\kappa^p$ . The evolution law of  $\kappa^p$  is given as,

$$\dot{\kappa}^p = \frac{\dot{\varepsilon}^p}{x_D(\bar{\xi})} [\Gamma(\cos \bar{\theta})]^2 \quad (24)$$

where  $\dot{\varepsilon}^p$  represents the Euclidean norm of the plastic strain rate tensor defined as  $\dot{\varepsilon}^p = \|\dot{\varepsilon}_{ij}^p\| = \sqrt{\dot{\varepsilon}_{ij}^p \dot{\varepsilon}_{ij}^p}$  and  $x_D(\bar{\xi})$  is the hardening ductility measure which encapsulate the influence of hydrostatic pressure on ductility. It is an increasing function of pressure (or decreasing function of  $\bar{\xi}$ ) and is defined by the peak value of total plastic strain when the failure envelope is reached (*i.e.* when  $\kappa^p = 1$ ) under triaxial compression loading condition. It is given as follows,

$$x_D(\bar{\xi}) = \begin{cases} A_D \exp(B_D R_D(\bar{\xi})) + C_D & \text{if } R_D(\bar{\xi}) > 0 \\ D_D \exp(E_D R_D(\bar{\xi})) + F_D & \text{if } R_D(\bar{\xi}) \leq 0 \end{cases} \quad (25)$$

where  $R_D$  varies linearly with  $\bar{\xi}$  defined as follows,

$$R_D(\bar{\xi}) = \frac{\bar{\xi}}{f_c} + \frac{1}{\sqrt{3}} \quad (26)$$

Function  $x_D$  has six parameters; two out of these six parameters, however, can be determined by imposing a condition of smooth transition at  $R_D = 0$ . This implies,

$$\begin{aligned} A_D + C_D &= D_D + F_D \\ A_D B_D &= D_D E_D \end{aligned} \quad (27)$$

Four remaining parameters can be calibrated from values of total plastic strains at peak stress under unconfined tension, unconfined compression, and compression under low and high confinement levels. [Eq. \(24\)](#) can also be used to define  $h^p(\bar{\sigma}_{ij}, \kappa^p)$  (see [Eq. \(7<sub>2</sub>\)](#) above) which is determined as follows,

$$h^p(\bar{\sigma}_{ij}, \kappa^p) = \frac{\|m(\bar{\sigma}_{ij}, \kappa^p)\|}{x_D(\bar{\sigma}_{ij} \delta_{ij} / \sqrt{3})} [\Gamma(\cos \bar{\theta})]^2 \quad (28)$$

Finally,  $q(\kappa^p)$  is defined in terms of  $\kappa^p$  as follows ([Grassl and Jirásek, 2006](#)),

$$q(\kappa^p) = \begin{cases} q_0 + (1 - q_0) [(\kappa^p)^2 - 3\kappa^p + 3] \kappa^p & \text{if } \kappa^p < 1 \\ 1 & \text{if } \kappa^p \geq 1 \end{cases} \quad (29)$$

Note that the minimum and maximum value of  $q(\kappa^p)$  is  $q_0$  and 1, respectively, and corresponding of  $\kappa^p$  is 0 and 1, respectively.

### 2.2.3. Non-associative plastic flow rule

The inelastic volumetric dilatancy is determined from the volumetric component of plastic strain increment. It has been reported that by using an associative flow rule, in which the direction of the plastic strain increment is normal to the yield surface, a significant overestimation of volumetric expansion for frictional material such as concrete is obtained under compressive stresses ([Etse and Willam, 1994](#); [Smith et al., 1989](#)). Similarly, the normality rule severely over-predicts the triaxial strength in strain controlled environments, as the excessive dilation converts into large over-prediction of lateral confinement ([Etse and Willam, 1994](#)). Therefore, to control the amount of dilatancy a non-associated flow rule is adopted in the present model. The plastic potential  $F^p$  is subsequently determined by using a volumetric modification of the yield function  $F$  in which the hydrostatic component of the plastic strain rate is the only one that does not follow the normality flow rule.  $F^p$  is given as follows,

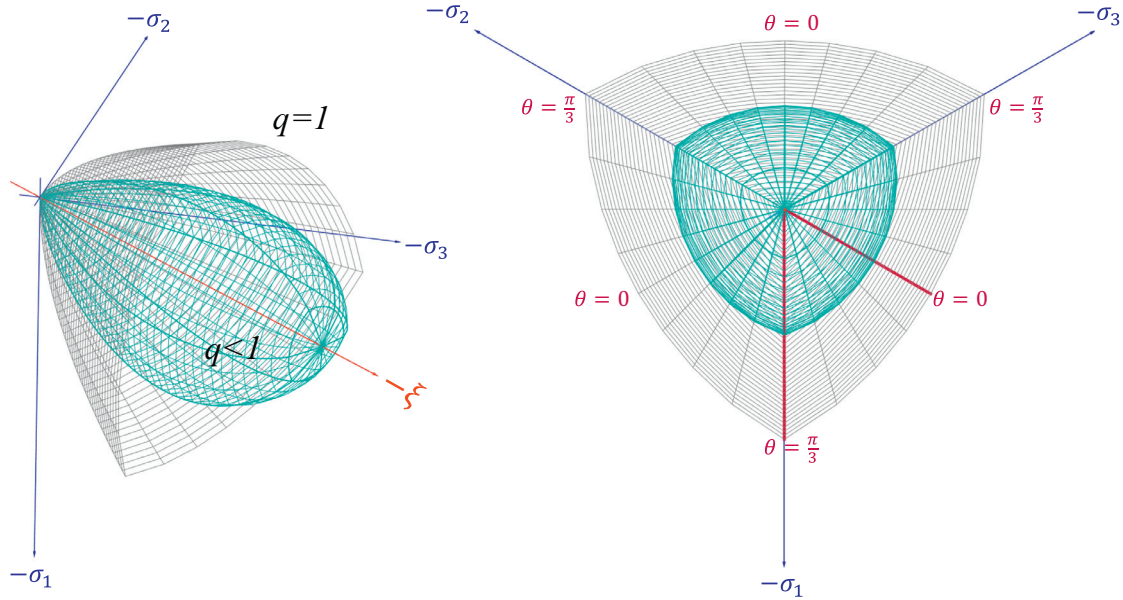


Fig. 4. Evolution of the of the yield surface  $F$  in principal stress space.

$$F^p(\bar{\xi}, \bar{\rho}, \bar{\theta}, q(\kappa^p)) = F(\bar{\xi}, \bar{\rho}, \bar{\theta}, q(\kappa^p)) + (q(\kappa^p))^2 f(\bar{\xi}, q(\kappa^p)) \quad (30)$$

where function  $f$ , which depends on the volumetric stress for a given level of hardening, is expressed as follows,

$$f(\bar{\xi}, q(\kappa^p)) = \left( A_f B_f \exp \frac{R_f(\bar{\xi})}{B_f} + C_f \frac{\bar{\xi}}{f_c} \right); \quad R_f(\bar{\xi}) = \frac{\bar{\xi} - \bar{\xi}_{vertex}}{f_c} \quad (31)$$

where  $\bar{\xi}_{vertex}$  represents the hydrostatic tensile strength given as  $\bar{\xi}_{vertex} = \frac{\sqrt{3}f_c}{m_0}$ .

The material parameters  $A_f$ ,  $B_f$  and  $C_f$  are determined from three different experiments with dilatancy measurements at different levels of confinement e.g. unconfined tension test, and compression tests under low and high confinement. Appendix C presents the gradient of the yield and plastic potential function.

### 2.3.3. Damage characterization

In the parlance of continuum damage mechanics, progressive loss of material integrity and stiffness degradation is a direct result of the growth and coalescence of micro-cracks, micro-voids and other distributed defects constituting overall damage. In this work the damage in the material is defined by an isotropic scalar parameter  $D$  which is a function of tensile and compressive damage parameters  $D^+$  and  $D^-$ , respectively. These parameters are functions of  $\kappa^+$  and  $\kappa^-$  ISVs, respectively. In this section we describe the relationship between these parameters and their corresponding ISVs, along with their evolution.

Under tensile loading, the specimen develops a localized fracture zone comprised of micro-cracks as the peak stress is realized. Upon continued loading, the unstable growth and eventual coalescence of micro-cracks in this fracture zone (which is usually narrow and is aligned perpendicular to tensile loading direction) cause a decrease in the load carrying capacity of the specimen which ultimately falls to zero. This corresponds to the post-peak softening part of the stress-strain curve. Consequently, the plastic strain rate is localized within this zone, separated from the remainder of the

body which experiences elastic unloading. In this work, we model this localized fracture zone as a fictitious cohesive crack whose response is characterized by a traction-separation law or a cohesive law. This law relates the traction transmitted by a partially formed cohesive crack to homogenized crack opening displacement (COD). In order to render objectivity to the damage model with respect to the size of finite element mesh (when  $C^0$  continuous finite elements are used), c.f. (Bazant and Oh, 1983; Oliver, 1989), COD is transformed into tensile fracture strain while incorporating it in to the constitutive model, by smearing it over a certain 'crack band width' which is considered to be an internal characteristic length denoted as  $l_c$ . We note that  $l_c$  represents a material property of a heterogeneous brittle/quasi-brittle material such as concrete that governs the minimum width of a zone of strain-softening damage in non-local continuum damage formulations (c.f. (Bazant and Pijaudier-Cabot, 1989)). It is a part of constitutive framework describing damage evolution; its incorporation in the model implies that there is a limit to the width of the localization zone preventing the damage from localizing to a zero volume. An estimate of  $l_c$  was made experimentally by Bazant and Pijaudier-Cabot (1989) to be  $\sim 2.7$  X maximum-aggregate-size of concrete. Therefore,  $l_c$  is interpreted as the damage zone size. However, in the context of finite element implementation, main problem caused by such strain softening models is spurious mesh sensitivity. If the length-scale parameter  $L$  (which is related to the finite element mesh size denoted by  $l_{FE}$ , order of the elements, orientation of the localization with respect to mesh boundaries, etc.) is not accounted for in the finite element model, total energy dissipated during damage evolution will depend on mesh density. One way is to make  $L$  equal to  $l_c$  in areas of localized cracking. However, as noted by Bazant (1986) making  $L$  equal to  $l_c$  is impractical for large structures as  $l_c$  can be very small compared to structure dimensions. Therefore instead of first identifying  $l_c$  of a material and enforcing  $L=l_c$ , the average stress-strain relation for the finite element is adjusted to account for the mesh-size effect to ensure the same energy dissipation, (i.e. the same fracture energy  $G_f^f$  for different element size  $l_{FE}$ ). Subsequently,  $l_c$  is interpreted as  $L$  during the implementation (c.f. (Lee and Fenves, 1998; Lubliner et al., 1989; Oliver, 1989; Voyiadjis et al., 2008)).

A more sophisticated remedy to overcome the pathological mesh dependence is by using a regularized integral type non-local formulation in which the interaction between neighboring points is also taken into account by weighted spatial averaging of the damage ISVs, *c.f.* (Pijaudier-Cabot and Bažant, 1987). This will be addressed in a forthcoming paper, alongside details related to the computational aspects - including integration algorithm and robustness - of the proposed model within the context of finite element implementation.

Denoting the stress transmitted across the surfaces of the fictitious crack (which represents the localized fracture zone) as  $\sigma_n$ , and the COD with respect to the displacement at the peak stress as  $u$ , the energy absorbed in the fracture zone during damage evolution under uniaxial tension is described as follows,

$$G_f^I = \int_0^{u_f} \sigma_n du \quad (32)$$

Eq. (32) also defines the fracture energy under mode-I cracking denoted by  $G_f^I$  which is a material property.  $u_f$  is the crack rupture opening with respect to the displacement at the peak stress when crack is fully formed and the traction  $\sigma_n = 0$ . Moreover, within the context of the smeared-crack concept, the mapping between  $u$  and tensile fracture strain represented by tensile damage ISV  $\kappa^+$  is given as follows,

$$u = l_c \kappa^+ \quad (33)$$

Next, the function  $\dot{F}^+$  is given as follows

$$\dot{F}^+ = \begin{cases} 0 & \text{if } \kappa^p < 1 \\ R(\bar{\sigma}_{ij}) \dot{\epsilon}^{p+} & \text{if } \kappa^p \geq 1 \end{cases} \quad (34)$$

where factor  $R(\bar{\sigma}_{ij})$  is defined by Eq. (4), and the equivalent plastic tensile strain rate  $\dot{\epsilon}^{p+} = \dot{\lambda} \|m_k\|$ ,  $k = 1, 2, 3$ , where  $\langle m_k \rangle$  are positive principal components of the gradient of plastic potential defining the flow direction (tensor  $m_{ij}$ , see Eq. (7<sub>1</sub>)). Note that during damage evolution,  $\dot{\kappa}^+ = \dot{F}^+$ .

Next, the cohesive law under tensile loading which describes the post peak softening response is considered to follow the exponential law given by,

$$\sigma_n = \bar{\sigma}_n (1 - D^+) = \bar{\sigma}_n \exp\left(-\frac{u}{u_t}\right) \quad (35)$$

where,  $\bar{\sigma}_n$  is the peak stress and  $u_t$  is the shape parameter controlling the slope of the softening curve. Parameter  $u_t$  can be derived by first substituting Eq. (33) in (30) and noting that  $u_f \rightarrow \infty$  for exponential law and  $\bar{\sigma}_n$  is equal to  $f_t$  under uniaxial tensile loading, to obtain the following,

$$G_f^I = f_t \int_0^\infty \exp\left(-\frac{u}{u_t}\right) du \quad (36)$$

Integrating and rearranging terms finally yields

$$u_t = \frac{G_f^I}{f_t} \quad (37)$$

Next, substituting Eq. (33) in (35), and using Eq. (37) we finally obtain the expression for  $D^+$  as follows,

$$D^+ = 1 - \exp\left(-\frac{f_t l_c}{G_f^I} \kappa^+\right) \quad (38)$$

The brittle fracture energy concept used for the tensile case is extended to the compressive stress states by accounting for the fact that unlike in the tensile case, the number of nucleated cracks which propagate and coalesce upon continued loading are much higher under compressive loading. Past experimental observations (*c.f.* (Sfer et al., 2002)) have indicated that under moderate confining pressures, mode of failure is characterized as

brittle propagation and coalescence of several distributed cracks inclined along the most compressive stress direction, with well-defined peak loads and smoothly descending post-peak stress-strain curves. This results from extensive microcracking coalescing into several macro-cracks along principal compressive stress direction. However, at high confinement, failure mode appears to be less brittle as the peak load increases and the steepness of the post-peak response decreases with an increase in the confining pressure, indicating an increase in the effective compressive strength and the ductility with increase in confinement (Sfer et al., 2002).

Considering these observations, the number of the fictitious cohesive cracks ( $N$ ) constituting localized fracture zone under triaxial compression with moderate confinement, on one hand, is considered to increase considerably with the increase in confining stress. On the other hand, at higher level of confinement (beyond brittle-to-ductile transition),  $N$  does not increase as rapidly with increase in confinement. In this study, we formulate  $N$  as a function of confinement under compressive loading using wing-crack micro-mechanics, which have been used numerous times in the past to study the failure behavior of brittle and quasi-brittle materials due to microcracking under compression (*c.f.* (Ashby and Sammis, 1990; Bhat et al., 2012; Deshpande and Evans, 2008; Horii and Nemat-Nasser, 1986; Paliwal and Ramesh, 2008)). Local inhomogeneities (including cavities, inclusions, regions in the vicinity of the interface between mortar and aggregates, etc.) in brittle and quasi-brittle materials *e.g.* rocks and concrete, serve as stress concentrators which promote micro-cracking ((Horii and Nemat-Nasser, 1986; Paliwal and Ramesh, 2008; Tapponnier and Brace, 1976)). Within this wing-crack framework, these stress concentrators are modeled as closed planar flaws embedded in elastic medium; frictional sliding of these flaws under external compressive loading give rise to local tensile stress field near the tips. Upon continued loading, the wing cracks sprout from each tip, and follow a path so as to maximize the mode-I stress intensity factor,  $K_I$  (for more details, refer to Bhat et al. (2012), Deshpande and Evans (2008) and Paliwal and Ramesh (2008)). This event is characterized as a nucleation of wing-micro-cracks. The nucleation criteria can be established by using the formulation described by Bhat et al. (2012) and Deshpande and Evans (2008), modified to account for triaxial compressive stress state, and is given as follows,

$$\frac{K_{IC}}{\sqrt{\pi a}} = \sqrt{\frac{4}{3}} \left( \sqrt{\frac{1 + \mu^2}{2}} \bar{\rho}_- + \frac{\mu}{2\sqrt{3}} \frac{\bar{\xi}_-}{\cos \bar{\theta}_-} \right) \quad (39)$$

where  $\mu$  is the friction coefficient, and  $\bar{\rho}_-$ ,  $\bar{\xi}_-$  and  $\bar{\theta}_-$  are functions of stress invariants (see Eq. 13) of the negative (or compressive) part of the effective stress tensor whose principal values are given as  $\langle \bar{\sigma}_i \rangle_-$ , where  $\langle x \rangle_- = \min(0, x)$  Eq. (39) can also be used to describe the minimum flaw size ( $2a_0$ ) which is nucleated (*i.e.* all cracks of size  $a \geq a_0$  in that specimen will be nucleated) if the specimen is subjected to a triaxial compressive stress state given as follows,

$$a_0 = \frac{(3/4\pi)K_{IC}^2}{\left( \sqrt{\frac{1 + \mu^2}{2}} \bar{\rho}_- + \frac{\mu}{2\sqrt{3}} \frac{\bar{\xi}_-}{\cos \bar{\theta}_-} \right)^2} \quad (40)$$

Next, we consider that these flaws are uniformly distributed in space but follow a certain size distribution given by a probability distribution function  $g(a)$ . Therefore, if total number of flaws in a specimen is denoted by  $\eta$ , and the maximum flaw size is  $2a_{max}$ , number of flaws of size  $a \geq a_0$  is given as,

$$N|_{a \geq a_0} = \eta \int_{a_0}^{a_{max}} g(a) da = \eta (1 - G(a_0)) \quad (41)$$

where  $G(a)$  is the cumulative distribution function. Assuming  $g(a)$  as one-parameter exponential distribution function,  $G(a_0)$  is given

as,

$$G(a_0) = 1 - \exp\left(-\frac{a_0}{a_m}\right) \quad (42)$$

where  $a_m$  is the mean flaw size. Substituting Eq. (40) in (42), and using Eq. (41) we obtain,

$$N|_{a \geq a_0} \equiv N(\bar{\rho}_-, \bar{\xi}_-, \bar{\theta}_-) = \eta \exp\left(-\frac{\beta}{\left(\sqrt{\frac{1+\mu^2}{2}} \frac{\bar{\rho}_-}{f_c} + \frac{\mu}{2\sqrt{3}} \frac{\bar{\xi}_-}{f_c \cos \theta_-}\right)^2}\right) \quad (43)$$

Where,

$$\beta = \left(\frac{3}{4\pi}\right) \frac{K_{IC}^2}{f_c^2 a_m} \quad (44)$$

Using Eq. (43), we can obtain number of fictitious cohesive cracks at the peak stress under uniaxial compression as follows,

$$N(-f_c, 0) = \eta \exp\left(-\frac{\beta}{\left[\left(\sqrt{\frac{1+\mu^2}{3}} - \frac{\mu}{3}\right)\right]^2}\right) \quad (45)$$

We note that  $N$  also serves as a ductility factor which has been used extensively in the past by several researchers while describing damage evolution under compressive stress states (c.f. (Etse and Willam, 1994; Folino and Etse, 2012; Grassl et al., 2013; Menétrey et al., 1997; Pramono and Willam, 1989)). Under compressive loading, decohesion accompanied by shear frictional sliding is precursor to nucleation of micro-cracks in the vicinity of numerous stress-concentration regions (including inclusions, interface regions between mortar, aggregates and other constituents). Therefore, the function  $\dot{\varepsilon}^{P-}$  which is used to define the compressive damage loading function (see Eq. (8)) is considered to be a function of equivalent plastic strain rate  $\dot{\varepsilon}^{P-}$ , parameter  $R$  (see Eq. (4)) and the ductility factor  $N$ , and is given as follows,

$$\dot{\varepsilon}^{P-} = \begin{cases} 0 & \text{if } \kappa^P < 1 \\ (1 - R(\bar{\sigma}_{ij})) \frac{\dot{\varepsilon}^{P-}}{N(\bar{\sigma}_{ij})} & \text{if } \kappa^P \geq 1 \end{cases} \quad (46)$$

where  $\dot{\varepsilon}^{P-} = \dot{\lambda} m_D$  is the equivalent deviatoric plastic strain rate and  $m_D$  is defined as,

$$m_D = \left\| m_{ij} - m_{kk} \frac{\delta_{ij}}{3} \right\| \quad (47)$$

During the damage evolution,  $\dot{\kappa}^- = \dot{F}^-$ . The damage law under compressive loading which describes the post peak softening response is defined as follows,

$$D^- = 1 - \left(1 + \frac{\kappa^-}{\kappa_c^-}\right) \exp\left(-\frac{\kappa^-}{\kappa_c^-}\right) \quad (48)$$

where,  $\kappa_c^-$  is the shape parameter. Similar to the tensile damage, compressive damage formulation can also be regularized as follows. First, analogous to Eq. (34), fracture energy under uniaxial compression loading is defined as

$$G_f^c = \int_0^{u_f^c} \sigma_c du = f_c \int_0^{u_f^c} (1 - D^-) du \quad (49)$$

where,  $\sigma_c$  is the equivalent stress under uniaxial compression (which is the absolute value of the axial stress) and  $u$  is the equivalent shear displacement with respect to its counterpart at the peak stress. It is related to the equivalent plastic shear strain accumulated after the peak stress smeared over the length  $l_c$ , as

$u(t) = l_c \int_{t_{peak}}^t [\dot{\varepsilon}^{P-}] dt = \int_{t_{peak}}^t [l_c (\dot{\lambda} m_D)] dt$  (time  $t = t_{peak}$  implies time at the peak stress). During damage evolution,  $\dot{\kappa}^- = \dot{F}^-$ ; using it with Eq. (47) and noting that  $R=0$ , we obtain the following,

$$u = l_c \kappa^- N(-f_c, 0) \quad (50)$$

Note that the length scale  $l_c$  is accounted for in the revised definition of  $D^-$  as follows,

$$D^- = 1 - \left(1 + \frac{u}{u_c}\right) \exp\left(-\frac{u}{u_c}\right) = 1 - \left(1 + \frac{l_c N(-f_c, 0) \kappa^-}{u_c}\right) \times \exp\left(-\frac{l_c N(-f_c, 0) \kappa^-}{u_c}\right) \quad (51)$$

where  $N(-f_c, 0)$  is given in Eq. (45), and parameter  $u_c$  can be obtained by substituting Eq. (51) in Eq. (49) and integrating as follows,

$$G_f^c = f_c \int_0^{\infty} \left(1 + \frac{u}{u_c}\right) \exp\left(-\frac{u}{u_c}\right) du \Rightarrow u_c = \frac{G_f^c}{2f_c} \quad (52)$$

Finally, substituting Eq. (52) in Eq. (51), the regularized damage law under compressive loading is obtained as follows,

$$D^- = 1 - \left(1 + \frac{2f_c l_c N(-f_c, 0) \kappa^-}{G_f^c}\right) \exp\left(-\frac{2f_c l_c N(-f_c, 0) \kappa^-}{G_f^c}\right) \quad (53)$$

### 3. Calibration of model parameters

Apart from elastic properties characterized by Young's modulus ( $E$ ) and Poisson's ratio ( $\nu$ ), other parameters used in this model can be categorized into three groups – parameters characterizing the evolution law of isotropic hardening ISV subsequently causing the evolution of the yield surface toward the failure surface, plastic potential defining the non-associative flow rule, and evolution laws of tensile and compressive ISVs describing the damage growth. All of these parameters can be determined using combinations of uniaxial tension, uniaxial compression, equibiaxial compression, and triaxial compression tests, which are discussed in this section.

Evolution law of hardening ISV  $\kappa^P$  incorporates a ductility measure  $x_D(\bar{\xi})$  which requires four independent parameters (see Eqs. (24)–(28)). These parameters can be determined by first computing the norm of the plastic strain tensor defined as  $\|\varepsilon_{ij}^P\| = \sqrt{\varepsilon_{ij}^P \varepsilon_{ij}^P}$  at the peak axial stress level obtained from uniaxial tension, uniaxial compression and triaxial compression tests at low and high confinement levels, and then calibrating both functions, as described in Eq. (25), using these data points. Fig. 5 shows the plot of both functions, parameters of which are obtained by calibrating unconfined and confined compression test data on high-strength concrete (HSC) from Lu et al. (2007). In the absence of uniaxial tension test data, plastic strain at the peak tensile stress is considered to be  $1 \times 10^{-5}$ . Finally, parameter  $q_0$  which is used in the formulation of hardening function (see Eq. 30) and defined as  $q_0 = \frac{f_{c0}}{f_c}$  where  $f_{c0}$  is elastic limit stress under uniaxial compression, can be determined from uniaxial compression test. Its default value is set as  $q_0=0.3$ .

Next, the function defining the failure surface (see Eq. 18) requires three parameters -  $f_c$ ,  $f_t$  and  $f_b$ . They can be determined from uniaxial compression, tension and equibiaxial compression tests, respectively. If appropriate experimental data to determine  $f_t$  and  $f_b$  is not available, they can be calibrated against  $f_c$  as follows -  $f_t = \frac{f_c}{10}$  and  $f_b = 1.16 f_c$  c.f. (Grassl et al., 2013; Papanikolaou and Kappos, 2007). Plastic potential function  $F^P$  additionally requires three parameters -  $A_f$ ,  $B_f$  and  $C_f$  (see Eqs. (30) and (31)). In this work,  $A_f$  and  $B_f$  are considered to be constants and  $C_f$  is considered

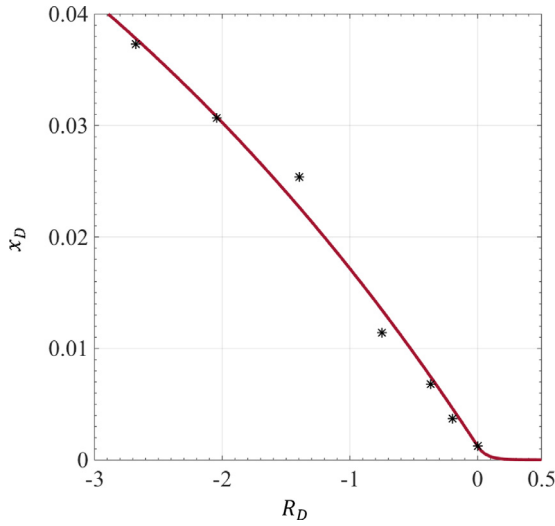


**Fig. 5.** Plot of calibrated ductility measure  $x_D$  vs. function  $R_D$  (see Eq. (28)) shown in solid line. Scattered data points are values of  $x_D$  (for various  $R_D$ ) obtained from triaxial compression experimental data on HSC reported by Lu et al. (2007).

to vary linearly with the hardening parameter  $q(\kappa^p)$  defined as  $C_f = c_1 + c_2 q(\kappa^p)$ . Experimental data from tension, and unconfined and confined compression tests is used to determine these parameters as follows. First, experimental values of incremental axial and lateral plastic strains are obtained as follows,

$$\Delta \varepsilon_a^p = \Delta \varepsilon_a - \Delta \bar{\sigma}_a / E; \quad \Delta \varepsilon_l^p = \Delta \varepsilon_l - \Delta \bar{\sigma}_l \nu / E \quad (54)$$

where subscripts  $a$  and  $l$  refer to axial and lateral, respectively, and the symbol  $\Delta$  is used to indicate the incremental values. Next, the incremental values of volumetric and deviatoric plastic strains are computed using Eq. (54) which is subsequently used to obtain the following relationship between  $\frac{\partial F^p}{\partial \xi}$  and  $\frac{\partial F^p}{\partial \bar{\rho}}$  as follows,

$$\begin{aligned} \Delta \varepsilon_{\xi}^p &= \Delta \lambda \frac{\partial F^p}{\partial \xi} = \frac{\Delta \varepsilon_a + 2\Delta \varepsilon_l}{\sqrt{3}}; \quad \Delta \varepsilon_{\bar{\rho}}^p = \Delta \lambda \frac{\partial F^p}{\partial \bar{\rho}} \\ &= \sqrt{\frac{2}{3}} |\Delta \varepsilon_a - \Delta \varepsilon_l| \Rightarrow \frac{\partial F^p}{\partial \xi} = \left( \frac{\partial F^p}{\partial \bar{\rho}} \right) \frac{\Delta \varepsilon_{\xi}^p}{\Delta \varepsilon_{\bar{\rho}}^p} \end{aligned} \quad (55)$$

After computing partial derivatives of  $F^p$  (see Eqs. (30) and (31)) and substituting in the equation above, we obtain the following equation for the gradient of the non-associative parameter  $f(\xi, q(\kappa^p))$  as follows,

$$\begin{aligned} \frac{df}{d\xi} &= A_f \exp \frac{R_f(\xi)}{B_f} + C_f (q(\kappa^p)) \\ &= \left[ \left( \frac{3\bar{\rho}}{q^2(\kappa^p) f_c} + \frac{m_0 \Gamma(\cos \bar{\theta}, e) F_c}{\sqrt{6}} \right) \frac{\Delta \varepsilon_{\xi}^p}{\Delta \varepsilon_{\bar{\rho}}^p} - \frac{m_0 \Gamma(\cos \bar{\theta}, e) \bar{\rho}}{\sqrt{6}} \right. \\ &\quad \left. \times \left( \frac{dF_c}{d\xi} \right) - 2 \left( \frac{m_0 \bar{\xi}}{\sqrt{3} f_c} - 1 \right) F_c \left( \frac{dF_c}{d\xi} \right) f_c - \frac{m_0 F_c^2}{\sqrt{3}} \right] \end{aligned} \quad (56)$$

Hence, once  $\Delta \varepsilon_{\xi}^p$  and  $\Delta \varepsilon_{\bar{\rho}}^p$  are determined from tensile and compression tests (which correspond to a given stress state), values of  $\xi$ ,  $\bar{\rho}$ ,  $\Gamma(\cos \bar{\theta}, e)$  are also known for each set of  $\Delta \varepsilon_{\xi}^p$ ,  $\Delta \varepsilon_{\bar{\rho}}^p$ . Using them,  $q(\kappa^p)$  is obtained such that  $F(\xi, \bar{\rho}, \bar{\theta}, q(\kappa^p)) = 0$ , which also give  $\xi_0(q(\kappa^p))$  and  $\xi_1(q(\kappa^p))$ . Using these values,  $F_c$  and  $\frac{dF_c}{d\xi}$  are also obtained. Hence, the right hand side (RHS) of Eq. (56) is completely determined. Finally, optimized set of parameters -  $A_f$ ,  $B_f$  and  $C_f$  are determined from values of RHS of Eq. (56). Note that in case tension test data is not available, compression tests under low, moderate and high confinement can also be used to obtain these parameters. Also note that the Lode angle  $\bar{\theta}$  is

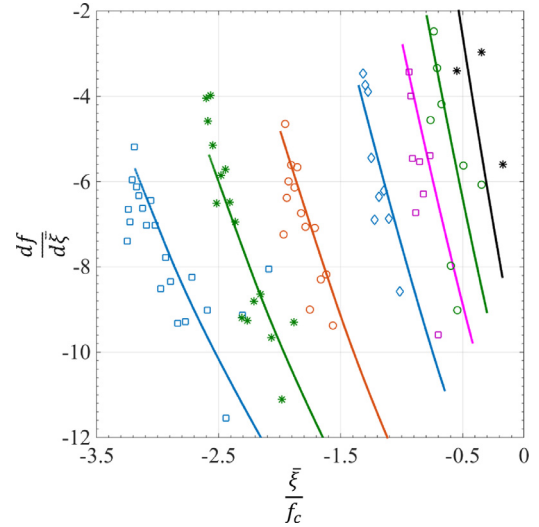


**Fig. 6.** Plots of calibrated  $\frac{df}{d\xi}$  vs.  $\frac{\xi}{f_c}$  (see Eq. (53)) shown in solid lines. Scattered data are obtained from triaxial compression experiments on HSC reported by Lu et al. (2007).

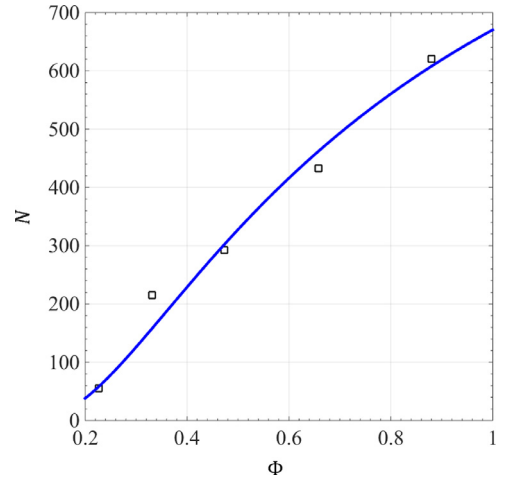


**Fig. 7.** Plot of calibrated  $N$  vs. the stress factor  $\Phi \equiv \left( \sqrt{\frac{1+\mu^2}{2}} \bar{\rho}_- + \frac{\mu}{2\sqrt{3}} \frac{\xi}{\cos \bar{\theta}} \right)^2$  (see Eq. (45)) shown in solid line. Scattered data points are values of  $N$  (for various  $\Phi$ ) obtained from triaxial compression experiments on HSC reported by Lu et al. (2007).

constant throughout each experiment needed to calibrate these parameters. Fig. 6 shows plots of  $\frac{df}{d\xi}$  vs.  $\xi$  (as scattered plots) computed from several triaxial compression experiments on HSC by Lu et al. (2007) on HSC under low, moderate and high confinement, and also shows plots of corresponding function calibrated using Eq. (56) above (shown as solid lines).

Finally, the damage is a function of tensile and compressive damage parameters  $D^+$  and  $D^-$ , respectively whose growth depends on the evolution of corresponding ISVs -  $\kappa^+$  and  $\kappa^-$ . The tensile damage parameter  $D^+$  requires a shape parameter  $u_t$  and a characteristic internal length scale parameter  $l_c$ . It is chosen to be 100 mm in this work, *c.f.* (Etse and Willam, 1994; Folino and Etse, 2012; Grassl et al., 2013).  $u_t$ , on the other hand, is determined from the fracture energy under mode-I cracking  $G_f^I$  using Eq. (37). Next, the compressive damage parameter  $D^-$  requires a ductility factor  $N(\bar{\sigma}_{ij})$ , which is a function of  $\eta$ ,  $\beta$  and  $\mu$ , and a shape parameter  $\kappa_c^-$ . These parameters are determined from the softening part of the stress and strain curves obtained from uniaxial and triaxial compression experiments. Note that  $D^-$  is a function of product of  $\eta$  and  $\kappa_c^-$ ; hence, unless the flaw density characterizing the parameter  $\eta$  is known *a priori*, a composite pa-

**Table 1**  
List of parameters used for each example.

	$E$ (Gpa)	$\nu$	$A_f$	$B_f$	$C_f$	$D_D$	$E_D$	$F_D$	$\eta$	$\beta$
Lu et al., (2007) $f_c = 68.6$ (Mpa)	33	0.14	10.03	1.05	$13.47q - 19.53$	-0.075	0.245	0.0764	1383	0.716
Imran and Pantazopoulou (1996) $f_c = 47.4$ (Mpa)	30	0.2	6.32	1.1	$15.7q - 19.7$	-0.106	0.213	0.1086	8473	1.2
Canar and Bažant. (2000) $f_c = 45.7$ (Mpa)	25	0.2	10.03	2.1	$13.43q - 22.53$	-0.25	0.045	0.2512	8473	1.8
Kupfer et al., (1969) $f_c = 32.8$ (MPa)	32	0.2	14.5	1.5	$2.86q - 16.36$	-0.09	0.25	0.0918	1993	0.92
Karsan and Jirsa (1969) $f_c = 27.5$ (MPa)	30	0.2	7.63	1.7	$3.14q - 12.8$	-0.09	0.2	0.0924	6315	1.25
	$E$ (Gpa)	$\nu$	$A_f$	$B_f$	$C_f$	$A_D$	$B_D$	$C_D$	$G_f$ (Jm <sup>-2</sup> )	
Gopalaratnam and Shah (1985) $f_c = 34.1$ (MPa)	31.7	0.2	11.32	1.7	$3.14q - 12.8$	0.00237	-7.39	$3 \times 10^{-5}$	45.33	

For all cases:  $q_0 = 0.3$ ,  $f_t = f_c/10$ ,  $f_b = 1.16f_c$ ,  $\mu = 0.6$ ,  $\kappa_c^- = 10^{-4}$ .

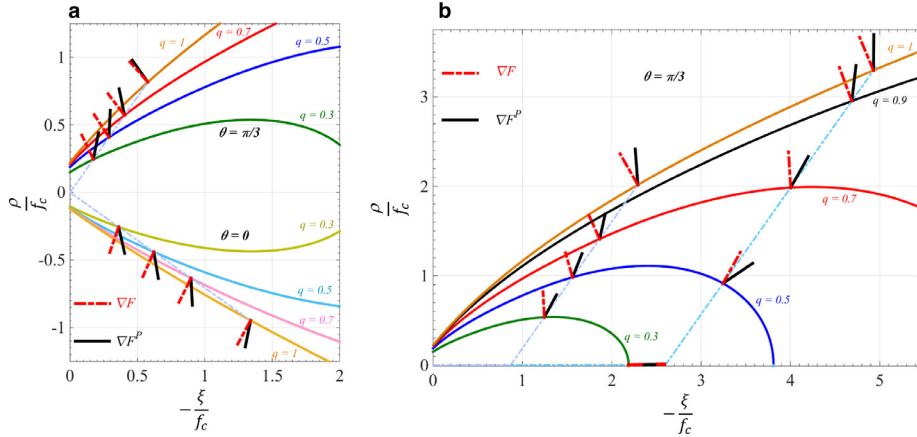


**Fig. 8.** Direction of plastic strain vector obtained using non-associative flow rule (shown in solid lines) compared with the direction of the gradient of the yield surface (shown in dashed lines) for (a) uniaxial and equibiaxial compression loading, and (b) triaxial compression loading under low and high confinement.

parameter  $\eta' = \eta\kappa_c^-$  is calibrated from these tests. Also note that the friction coefficient in such quasi-brittle materials including rocks is difficult to measure using standard laboratory tests, and is typically considered to be closer to 0.6, c.f. (Ashby and Sammis, 1990; Bhat et al., 2012; Kachanov, 1982; Paliwal and Ramesh, 2008). In order to calibrate  $\eta'$  and  $\beta$ ,  $N'(\bar{\sigma}_{ij}) = N(\bar{\sigma}_{ij})\kappa_c^-$  is first obtained from the softening part of stress-strain curves;  $\eta'$  and  $\beta$  are then determined by calibrating the values using Eq. (41). Fig. 7 shows scattered plot of  $N$  as a function of stress-factor denoted by  $\Phi \equiv (\sqrt{\frac{1+\mu^2}{2} \frac{\bar{\rho}_-}{f_c} + \frac{\mu}{2\sqrt{3}} \frac{\bar{\xi}_-}{f_c \cos\theta_-}})^2$  for  $\mu = 0.6$  and  $\kappa_c^- = 10^{-4}$  using triaxial compression experimental data reported by Lu et al. (2007); alongside is the fitted plot obtained by using the function given in Eq. (43).

Using the above calibration procedure, the gradient directions of the yield (shown as dashed lines) and of the plastic potential surfaces (shown as solid lines) at various hardening levels in the Rendulic plane are shown in Fig. 8 depicting non-associative characteristics of the plastic flow. Fig. 8(a) describes the scenario for uniaxial and equibiaxial compression loading, and Fig. 8(b) describes it for triaxial compression loading under low- and high confinement. As can be inferred from the plots, the hydrostatic component of the plastic strain vector (gradient direction of plastic potential) is less inclined toward the positive hydrostatic axis compared with the hydrostatic component of the gradient direction of the yield surface, suggesting slower accumulation of the plastic volumetric strains. This also suggest that an associated flow rule would result in an overestimation of the plastic dilatancy of this high strength concrete.

**4. Model comparison with experimental results**

In this section, we describe several numerical examples under different loading conditions using the proposed model on both normal and high strength concrete. Model results are compared with experimental data reported in the literature, as well as with

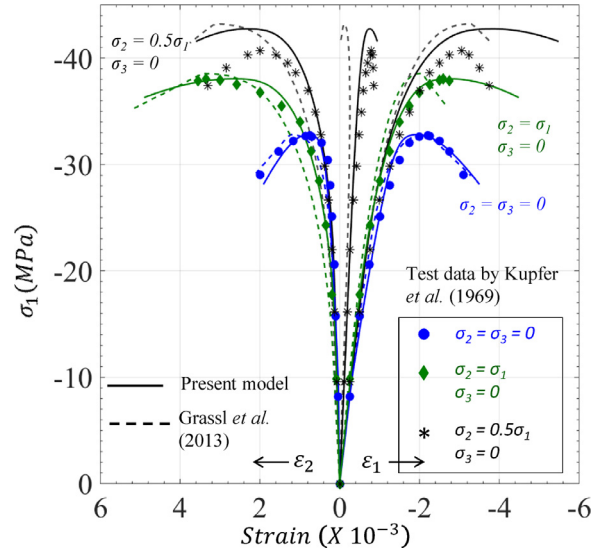


**Fig. 9.** Plots of axial stress ( $\sigma_1$ ) vs. axial and lateral strain ( $\epsilon_1$  and  $\epsilon_2$ , respectively) under uniaxial and biaxial stress states obtained by using present model and using model by Grassl et al. (2013) compared with the experimental results by Kupfer et al. (1969).

other model predictions proposed more recently. Table 1 lists all parameters used for each example.

First, the model results are compared with uniaxial and biaxial compression experimental results by Kupfer et al. (1969), alongside the response predicted by Grassl et al. (2013) as shown by solid and dashed lines, respectively in Fig. 9. Next, the model predictions are compared with results from triaxial compression experiments conducted by Imran and Pantazopoulou (1996) where the lateral confinement was varied from 0 to 43.2 MPa, and also compared with corresponding model response by Grassl et al. (2013).

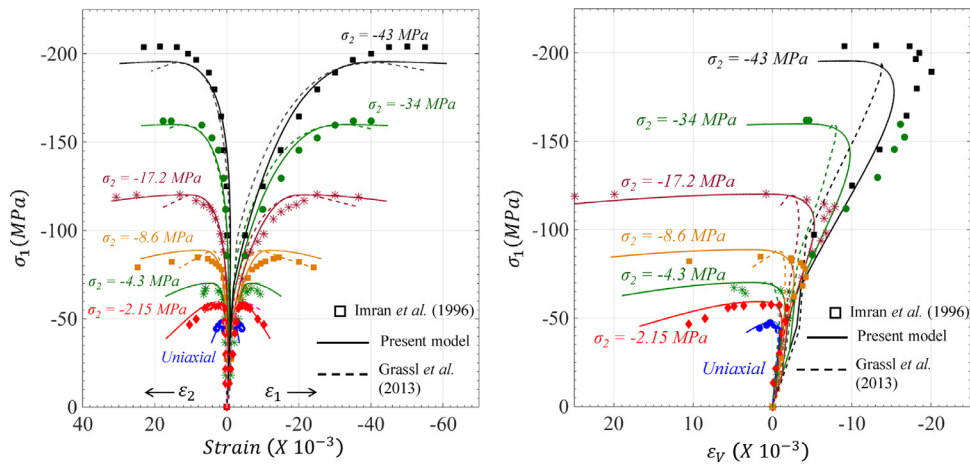


Fig. 10. Plots of (a) axial stress ( $\sigma_1$ ) vs. axial and lateral strain ( $\epsilon_1$  and  $\epsilon_2$ , respectively), and (b) axial stress ( $\sigma_1$ ) vs. volumetric strain ( $\epsilon_V$ ) under triaxial compressive stress states obtained by using present model and using model by Grassl et al. (2013) compared with the experimental results by Imran and Pantazopoulou (1996).

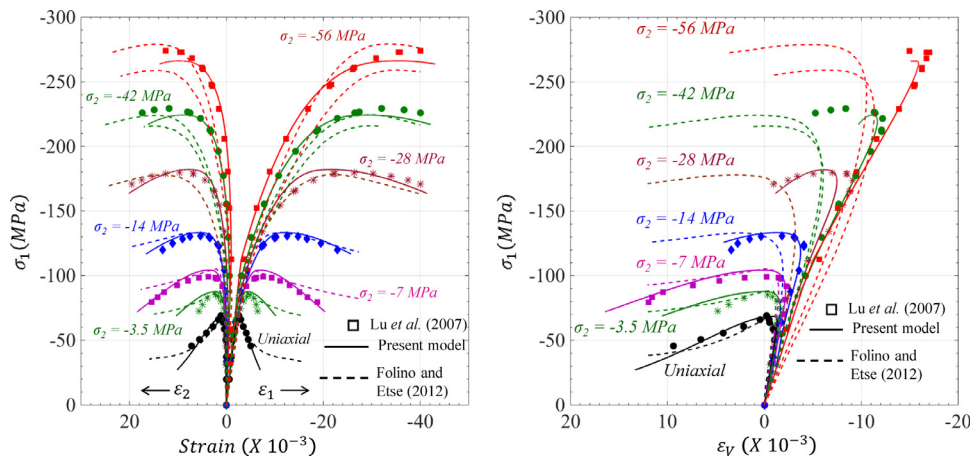


Fig. 11. Plots of (a) axial stress ( $\sigma_1$ ) vs. axial and lateral strain ( $\epsilon_1$  and  $\epsilon_2$ , respectively), and (b) axial stress ( $\sigma_1$ ) vs. volumetric strain ( $\epsilon_V$ ) under triaxial compressive stress states obtained by using present model and using model by Folino and Etse. (2012) compared with the experimental results on HSC by Lu et al. (2007).

Fig. 10(a) and (b) show the plots of axial stress vs. axial and lateral strain and axial stress vs. volumetric strain, respectively under varying confinement levels.

Fig. 11(a) and (b) show model results in the form of both, axial stress vs. axial and lateral strain and axial stress vs. volumetric strain, compared with another triaxial compression experimental results on high-strength concrete as reported by Lu et al. (2007) under various confinement levels ranging from 0 to 82% of its uniaxial compressive strength. Results, shown in solid lines, are also compared with the prediction of a model proposed recently by Folino and Etse (2012) as shown by dashed lines in the figure. Next, in Fig. 12(a) and (b), model results are compared with experimental results reported by Caner and Bažant (2000) on concrete subjected to triaxial compression under very high lateral confinement (as high as  $\sim 900\%$  of  $f_c$ ), and subjected to pure hydrostatic compression. They are also compared with previous model predictions by Grassl et al. (2013).

As is quite apparent from all these results, predictions of proposed model are in very good agreement with the experimental results on concrete undergoing biaxial and triaxial compression during both, pre-peak hardening and post peak softening stages under low, moderate and high confinement range. It is also noted that model predicts the axial stress vs. volumetric strain during triaxial compression loading particularly well under both low and high confinement compared with previous model predictions.

Model results were also compared with the cyclic uniaxial tensile and compressive loading-unloading and reloading experimental data as reported by Gopalratnam and Shah (1985) and by Karsan and Jirsa (1969), respectively. As shown in Fig. 13(a) and (b), model response agrees quite well with the experimental results, and satisfactorily reproduces the experimentally observed post peak softening behavior along with stiffness degradation and irreversible (residual) strains upon unloading.

Finally, we illustrate the model response under two loading cases – biaxial tension-shear loading describing the shear behavior of the cracked material, and cyclic tension-compression loading. The results for the first case are shown in Fig. 14 in which both the tensile and the shear stress (denoted by  $\bar{\sigma}_{11}$  and  $\bar{\sigma}_{12}$ , respectively) normalized by  $f_c$  are plotted as a function of the sum of the axial and the shear strain (denoted by  $\epsilon_{11}$  and  $\epsilon_{12}$ , respectively). This case simulates the scenario in which a specimen is subjected to uniaxial tension and later subjected to shear under constant strain rate. The solid-blue curve shown in Fig. 14 represent the tensile stress as a function of strain. This plot shows that upon tensile loading (from point a to point c),  $\bar{\sigma}_{11}$  increases and reaches the peak (point b) and then it starts to decrease, and thereby the tensile damage is induced in the specimen. Note that Both  $\epsilon_{12}$  and  $\bar{\sigma}_{12}$  are zero during this time as shown by the dashed-red plot between points a and c. After the loading state at point c (see the shaded region in Fig. 14), the tensile strain is held fixed and the specimen is subjected to shear loading. Fig. 14 shows that upon shear

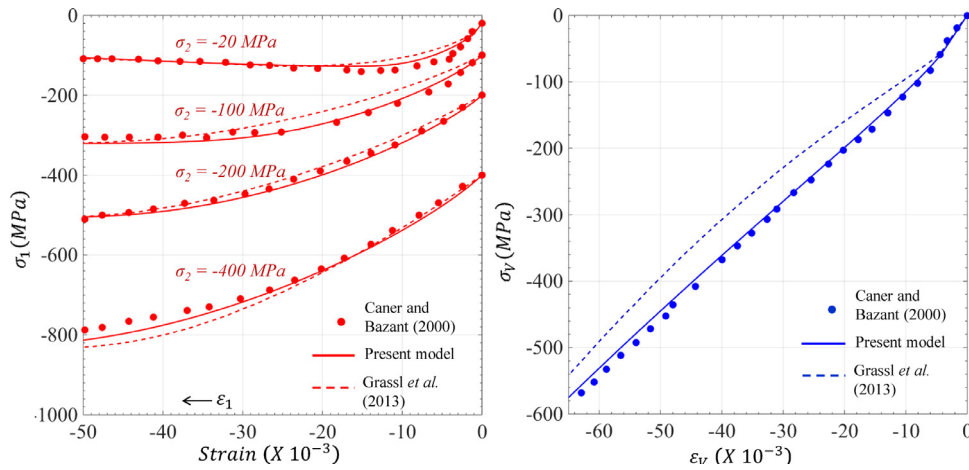


Fig. 12. Plots of (a) axial stress ( $\sigma_1$ ) vs. axial strain ( $\epsilon_1$ ), and (b) hydrostatic stress ( $\sigma_v$ ) vs. volumetric strain ( $\epsilon_v$ ) under triaxial compressive stress states obtained by using present model and using model by Grassl et al. (2013) compared with the experimental results by Caner and Bazant (2000).

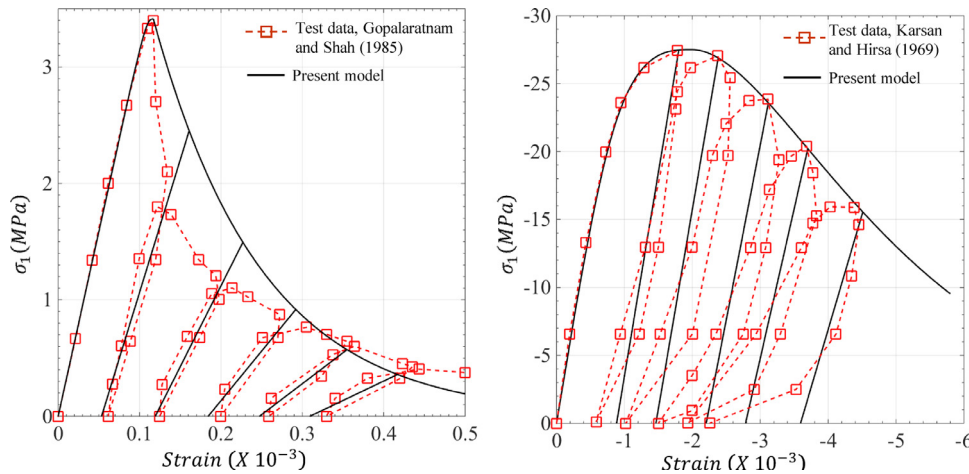


Fig. 13. Plots of axial stress ( $\sigma_1$ ) vs. axial strain under (a) cyclic uniaxial tensile, and (b) cyclic uniaxial compressive loading, obtained by using present model compared with experimental results by (a) Gopalaratnam and Shah (1985), and (b) Karsan and Hirsra (1969).

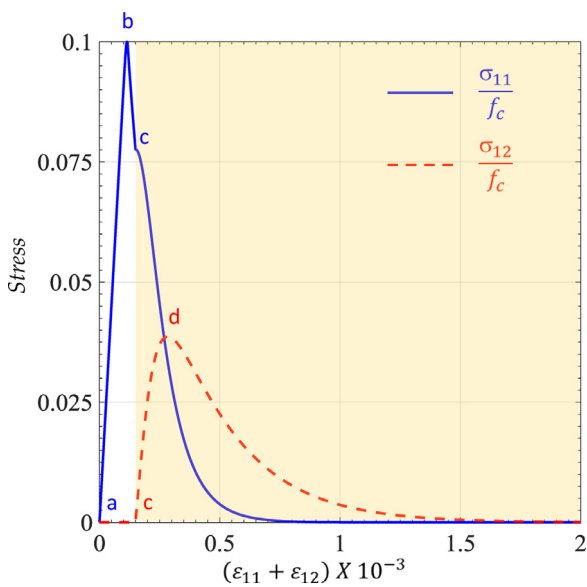


Fig. 14. Model response under biaxial tension-shear loading describing the shear behavior of the cracked material (shaded region depicts the response as a result of shearing after tensile loading).

loading,  $\bar{\sigma}_{11}$  continues to decrease toward zero, while  $\bar{\sigma}_{12}$  begins to increase, reaches the peak level (represented by point *d*) and then decreases toward zero.

Results for the second loading case are shown in Fig. 15 in which the axial stress,  $\sigma_1$ , normalized by  $f_c$  is plotted against the axial strain,  $\epsilon_1$  for three values of  $s_0$  (the parameter which influences the stiffness recovery factor  $s(\bar{\sigma}_{ij})$ ; see Eq. (3) and (4)). This case simulates the scenario in which the specimen is first subjected to uniaxial tension which results in the increase in  $\bar{\sigma}_1$  till it reaches the tensile strength (loading state from points *a* to point *b* as shown in Fig. 15). Upon continued loading,  $\sigma_1$  decreases and at point *c*, the unloading is initiated by reversing the direction of strain rate to negative. Note that due to the tensile damage evolution (from point *b* to point *c*), the value of the unloading slope, which denotes the unloading stiffness denoted by  $E^+$ , is less than the elastic stiffness of the undamaged material which is the effective elastic stiffness denoted by  $\bar{E}$ . Specimen is fully unloaded at point *d* (see the inset on the right in Fig. 15), after which compression is initiated. It is apparent from Fig. 15 that as the loading changed from tension to compression, specimen experienced the stiffness reduction degree which depends on parameter  $s_0$  (also see Eq. (3)). Fig. 15 shows that for  $s_0 = 1$  and  $s_0 = 0$ , there is no stiffness recovery, i.e.  $E^- = E^+$  (see the plot in solid-red line) and full stiffness recovery i.e.  $E^- = \bar{E}$  (see the plot in dashed-black line), respectively, where  $E^-$  is the elastic stiffness under compression. Fi-

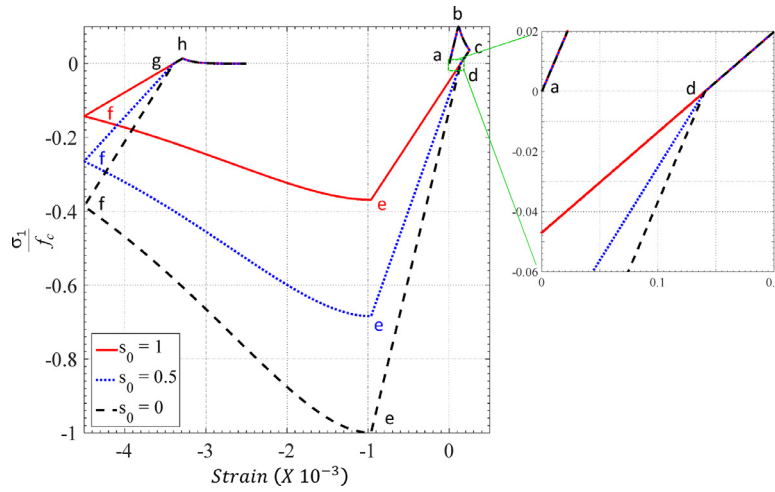


Fig. 15. Model response under cyclic uniaxial tension-uniaxial compression loading.

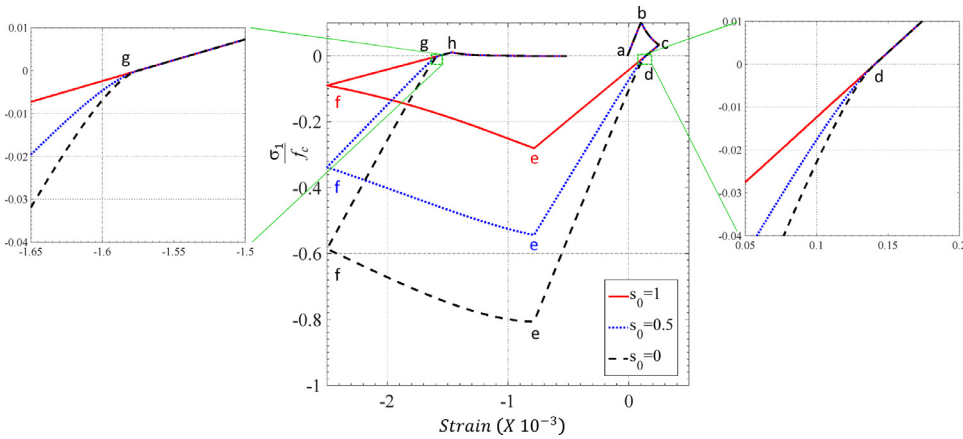


Fig. 16. Model response under cyclic tension-compression loading in which the lateral stresses are kept constant at  $\frac{f_c}{4}$ .

nally, for  $s_0=0.5$ ,  $E^+ < E^- < \bar{E}$  (see the plot in dotted-blue line). Upon continued loading, the compressive stress increases linearly with the axial strain, till it reaches the compressive strength (see point *e* in the plot), after which plasticity under compression commences. It subsequently results in softening, and upon continued loading, the compressive stress decreases and at point *f* the unloading is initiated (by again reversing the direction of strain rate to positive). The specimen is eventually completely unloaded (see point *g*) and subsequently, tension is initiated. Note that  $s=1$  under tension (see Eq. (4)), therefore the stiffness under tension upon load reversal (from compression-to-tension in the second cycle) is identical irrespective of  $s_0$ . Upon continued loading under tension, stress increases linearly with strain until the tensile strength is reached (see point *h*), after which softening commences and stress decreases toward zero. Note that as lateral stresses are zero in this case,  $s$  changes by a jump from 1 to  $s_0$  when the stress state changes from uniaxial tension to uniaxial compression (see the inset in Fig. 15).

Fig. 16 presents a similar cyclic tension-compression loading case in which the lateral stresses are non-zero and are kept constant at  $\frac{f_c}{4}$ . This allows  $s$  to vary continuously during the transition at point *d* (see the inset on the right in Fig. 16). In this case, the value of  $R$  (see Eq. (4)) changes continuously from 1 (at *d*) to  $\frac{1}{1 + 2\frac{\bar{\sigma}_{Ac}}{f_c}}$  as the axial stress turns compressive (where  $\bar{\sigma}_{Ac}$  represents the effective axial compressive stress value after the transition at *d*). Due to this continuous change in  $R$ , parameter

$s$  changes from 1 to  $s_0 + (1 - s_0)\frac{1}{1 + 2\frac{\bar{\sigma}_{Ac}}{f_c}}$  (at *d*) and the slope of the stress-strain curve varies continuously as the axial stress turns compressive. Note that for  $s_0 < 1$ , slopes of the stress-strain curves are higher suggesting higher elastic-stiffness in the compression-region compared with the tension-region (see the inset on the right in Fig. 16). Also note that at point *g* (see the inset on the left in Fig. 16 for details),  $R$  continuously increase to 1 and consequently  $s$  continuously changes from  $s_0 + (1 - s_0)R$  to 1 as axial stress changes from compression to tension, respectively. Therefore, similar to the uniaxial case in Fig. 15, all three plots coincide and are linear in the tension-region.

Finally, Fig. 17 presents a similar cyclic tension-compression loading case in which the lateral stresses are non-zero and are kept constant at  $-\frac{f_c}{4}$ . In this case,  $D = 1 - (1 - sD^+)(1 - D^-)$  where both  $D^+$  and  $D^-$  are non-zero between *b* and *d*.  $R$  is constant between *b* and *c* and is equal to  $\frac{2\frac{\bar{\sigma}_{At}|_b}{f_c}}{1 + 2\frac{\bar{\sigma}_{At}|_b}{f_c}}$  where  $\bar{\sigma}_{At}|_b$  is the peak tensile stress at *b*. Therefore parameter  $s$  is also constant between *b* and *c* and is equal to  $s_0 + (1 - s_0)\frac{2\frac{\bar{\sigma}_{At}|_b}{f_c}}{1 + 2\frac{\bar{\sigma}_{At}|_b}{f_c}}$ ; unlike previous cases, the overall damage evolution between *b* and *c* becomes a function of parameter  $s_0$  ( $D$  becomes an increasing function of  $s_0$ ). This is demonstrated in the inset on the top-right of Fig. 17 which shows the details of tensile softening curves dependence on parameter  $s_0$ .

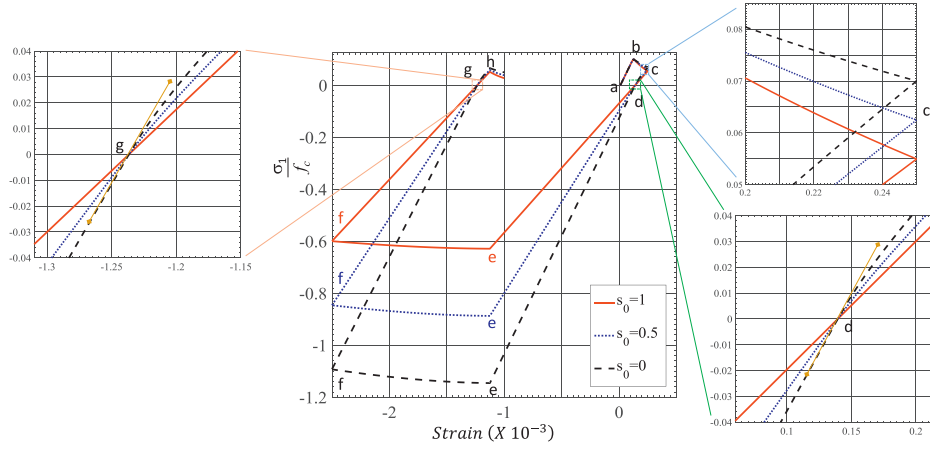


Fig. 17. Model response under cyclic tension-compression loading in which the lateral stresses are kept constant at  $-\frac{f_c}{4}$ .

Next,  $R$  changes continuously from  $\frac{2\frac{\sigma_{At}}{f_t}}{1+2\frac{\sigma_{At}}{f_t}}$  to 0 (at  $d$ ) as axial stress turns compressive ( $\bar{\sigma}_{At}$  is the effective axial tensile stress value before the transition at  $d$ ). Consequently, parameter  $s$  changes continuously from  $s_0 + (1-s_0)\frac{2\frac{\sigma_{At}}{f_t}}{1+2\frac{\sigma_{At}}{f_t}}$  to  $s_0$  at  $d$  and the slope of the stress strain curve varies continuously as the axial stress turns compressive (see the inset on the bottom-right in Fig. 17). Note that the stress-strain curves in the compression region (after  $d$ ) are linear with different slopes (depending on value of  $s_0$ ) and for  $s_0 < 1$ , their slopes are higher suggesting higher stiffness in the compression-region compared with the tension-region (see square-connected yellow guide-line in the inset). Also note that at  $g$  (see the inset on the left in Fig. 17 for details),  $R$  continuously increase from 0 and consequently  $s$  continuously changes from  $s_0$  to  $s_0 + (1-s_0)R$  as axial stress changes from compression to tension, respectively. Therefore, for  $s_0 < 1$ , the stress-strain plots are non-linear with lower slopes in the tension-region compared with the compression-region at  $g$ .

### 5. Summary

A new model for cementitious materials based on flow theory of plasticity and continuum damage mechanics is developed which excellently addresses major characteristics of their inelastic behavior e.g. confinement sensitive hardening and strain softening, pre- and post-peak volumetric behavior including post-peak dilatancy, stiffness degradation, brittle-ductile transition, and limitation of hardening in hydrostatic compression. Compared with recently reported models, the present model responses are in much better agreement with experimental results on different concretes subjected to various loading conditions including triaxial compression under low and high confinement.

### Acknowledgments

This work was performed under the auspices of the Center for Advanced Vehicular Systems (CAVS) at Mississippi State University and sponsored by the Engineering Research & Development Center under Cooperative Agreement number W912HZ-15-2-0004. The views and conclusions contained herein are those of the authors and should not be interpreted as necessarily representing the official policies or endorsements, either expressed or implied, of the Engineering Research & Development Center or the U.S. Government.

### Appendix A

After time-differentiating Eq. (11) and using Eqs. (2) and (12), we obtain

$$\begin{aligned} \dot{\sigma}_{ij} = & (1-D)\dot{\bar{\sigma}}_{ij} - \dot{D}\bar{\sigma}_{ij} = (1-D)\bar{C}_{ijkl}^{ep}\dot{\epsilon}_{kl} \\ & + \bar{\sigma}_{ij} \left[ (1-sD^+) \left( -\frac{\partial D^-}{\partial \kappa^-} \dot{\kappa}^- \right) + (1-D^-) \left( -s \frac{\partial D^+}{\partial \kappa^+} \dot{\kappa}^+ \right) \right. \\ & \left. + (1-D^-) \left( -D^+ \frac{\partial s}{\partial \bar{\sigma}_{mn}} \dot{\bar{\sigma}}_{mn} \right) \right] \end{aligned} \quad (A1)$$

During damage evolution, from Eq. (9) we have  $\dot{\kappa}^\pm = \dot{F}^\pm$ . Using Eqs. (34) and (46) and substituting them in Eq. (A1), we further obtain the following relationship

$$\begin{aligned} \dot{\sigma}_{ij} = & (1-D)\bar{C}_{ijkl}^{ep}\dot{\epsilon}_{kl} \\ & + \bar{\sigma}_{ij} \left[ (1-sD^+) \left( -\frac{\partial D^-}{\partial \kappa^-} H(\kappa^p - 1) \dot{\lambda} (1-R(\bar{\sigma})) \frac{m_D}{N(\bar{\sigma})} \right) \right. \\ & \left. + (1-D^-) \left( -s \frac{\partial D^+}{\partial \kappa^+} H(\kappa^p - 1) \dot{\lambda} R(\bar{\sigma}) \langle m_r \rangle \right) \right. \\ & \left. + (1-D^-) \left( -D^+ \frac{\partial s}{\partial \bar{\sigma}_{mn}} \dot{\bar{\sigma}}_{mn} \right) \right] \end{aligned} \quad (A2)$$

See Eq. (34) and Eqs. (46, 47) for the definitions of  $m_D$  and  $\langle m_r \rangle$  (where  $r=1, 2, 3$ ), respectively. Function  $H(x)$  in Eq. (A2) is the Heaviside step function which is equal to 1 if  $x > 0$  and is equal to 0 otherwise.  $R(\bar{\sigma})$  and  $N(\bar{\sigma})$  are given in Eqs. (4) and (43), respectively. Values of  $\frac{\partial D^+}{\partial \kappa^+}$  and  $\frac{\partial D^-}{\partial \kappa^-}$  are obtained from Eqs. (38) and (53), respectively and are given as follows

$$\begin{aligned} \frac{\partial D^+}{\partial \kappa^+} = & \frac{f_t l_c}{G_f^l} \exp\left(-\frac{f_t l_c}{G_f^l} \kappa^+\right); \quad \frac{\partial D^-}{\partial \kappa^-} = \left( \frac{2f_c l_c N(-f_c, 0)}{G_f^c} \right)^2 \kappa^- \\ & \times \exp\left(-\frac{2f_c l_c N(-f_c, 0)}{G_f^c} \kappa^-\right) \end{aligned} \quad (A3)$$

Let  $\bar{\sigma}_A$  ( $A = 1, 2, 3$ ) represent the principal values of the stress ( $\bar{\sigma}_{ij}$ ) tensor and the principal directions are denoted by  $n_i^{(A)}$ ,  $i = 1, 2, 3$ . Using spectral decomposition and using Eqs. (4) and (5) along with few algebraic manipulations we obtain the following

$$\frac{\partial s}{\partial \bar{\sigma}_{ij}} = \sum_{A=1}^3 \frac{\partial s}{\partial \bar{\sigma}_A} n_i^{(A)} n_j^{(A)} = (1-s_0) \sum_{A=1}^3 \frac{\partial R}{\partial \bar{\sigma}_A} n_i^{(A)} n_j^{(A)} \quad (A4)$$

where,

$$\frac{\partial R}{\partial \bar{\sigma}_A} = \frac{H(\bar{\sigma}_A)}{\sum_{B=1}^3 [2H(\bar{\sigma}_B)\bar{\sigma}_B - \bar{\sigma}_B]} - \frac{(2H(\bar{\sigma}_A) - 1) \sum_{B=1}^3 [H(\bar{\sigma}_B)\bar{\sigma}_B]}{\left(\sum_{B=1}^3 [2H(\bar{\sigma}_B)\bar{\sigma}_B - \bar{\sigma}_B]\right)^2} \quad (\text{A5})$$

Next, using Eq. (11) for  $\dot{\lambda}$  and substituting them in Eq. (A2), we finally obtain the following

$$\begin{aligned} \dot{\sigma}_{ij} = & (1-D)\bar{C}_{ijkl}^{ep}\dot{\epsilon}_{kl} \\ & + \bar{\sigma}_{ij} \left[ \left\{ (1-sD^+) \left( -\frac{\partial D^-}{\partial \kappa^-} H(\kappa^p - 1)(1-R(\bar{\sigma})) \frac{m_D}{N(\bar{\sigma})} \right) \right. \right. \\ & + (1-D^-) \left( -s \frac{\partial D^+}{\partial \kappa^+} H(\kappa^p - 1)R(\bar{\sigma})m_r \right) \left. \right\} \frac{1}{\psi} \frac{\partial F}{\partial \bar{\sigma}_{pq}} E_{pqkl}^0 \\ & + (1-D^-) \left( -D^+ \frac{\partial s}{\partial \bar{\sigma}_{mn}} \right) \bar{C}_{mnlk}^{ep} \left. \right] \dot{\epsilon}_{kl} = C_{ijkl}^{ep} \dot{\epsilon}_{kl} \end{aligned}$$

Therefore, effective elastoplastic tangent modulus  $C_{ijkl}^{ep}$  is finally obtained as

$$\begin{aligned} C_{ijkl}^{ep} = & (1-D)\bar{C}_{ijkl}^{ep} \\ & + \bar{\sigma}_{ij} \left[ \left\{ (1-sD^+) \left( -\frac{\partial D^-}{\partial \kappa^-} H(\kappa^p - 1)(1-R(\bar{\sigma})) \frac{m_D}{N(\bar{\sigma})} \right) \right. \right. \\ & + (1-D^-) \left( -s \frac{\partial D^+}{\partial \kappa^+} H(\kappa^p - 1)R(\bar{\sigma})m_r \right) \left. \right\} \frac{1}{\psi} \frac{\partial F}{\partial \bar{\sigma}_{pq}} E_{pqkl}^0 \\ & + (1-D^-) \left( -D^+ \frac{\partial s}{\partial \bar{\sigma}_{mn}} \right) \bar{C}_{mnlk}^{ep} \left. \right] \quad (\text{A6}) \end{aligned}$$

where  $\frac{\partial D^+}{\partial \kappa^+}$  and  $\frac{\partial D^-}{\partial \kappa^-}$  are given in Eq. (A3), and  $\frac{\partial s}{\partial \bar{\sigma}_{mn}}$  is given in Eq. (A4).

## Appendix B

### B.1. Determining $\bar{\xi}_0(q(\kappa^p))$

The point where the yield surface, for a given hardening parameter  $q(\kappa^p)$  (subsequently referred as  $q$ ), intersect the negative  $\bar{\xi}$  - axis is given by the stress coordinate  $(\bar{\xi}_0(q), 0)$  (subsequently referred as  $(\bar{\xi}_0, 0)$  from here onwards). It satisfies the yield function equation given by Eq. (23) This results in a quartic equation in  $\bar{\xi}_0$  which reads,

$$(1-q)^2 \left( \frac{\bar{\xi}_0}{\sqrt{3}f_c} \right)^4 + m_0q^2 \left( \frac{\bar{\xi}_0}{\sqrt{3}f_c} \right) - q^2 = 0 \quad (\text{B1})$$

Eq. (B1) has four roots. As its discriminant is less than zero, two of the roots imaginary and complex conjugate to each other; the third and the fourth roots are positive and negative real numbers, respectively. In order to determine them, we define the following,

$$\begin{aligned} d_0 = & -\frac{4}{3}q^2(1-q)^2; \quad d_1 = m_0^2q^4(1-q)^2; \quad d_2 = \frac{9m_0q^2}{\sqrt{3}(1-q)^2} \\ Q = & \left( \frac{d_1 + \sqrt{d_1^2 - 4d_0^3}}{2} \right)^{\frac{1}{3}} \\ S = & \frac{1}{2(1-q)} \sqrt{3 \left( Q + \frac{d_0}{Q} \right)} \\ p_1 = & -4S^2 + \frac{d_2}{S}; \quad p_2 = -4S^2 - \frac{d_2}{S} \quad (\text{B2}) \end{aligned}$$

Four roots of Eq. (B1) are given as,

$$\begin{aligned} \bar{\xi}_{0_1} = & -S - \frac{1}{2}\sqrt{p_1}; \quad \bar{\xi}_{0_2} = -S + \frac{1}{2}\sqrt{p_1} \\ \bar{\xi}_{0_3} = & -S - \frac{1}{2}\sqrt{p_2}; \quad \bar{\xi}_{0_4} = -S + \frac{1}{2}\sqrt{p_2} \quad (\text{B3}) \end{aligned}$$

as  $p_1 > 0$ , roots  $\bar{\xi}_{0_1}$  and  $\bar{\xi}_{0_2}$  are real, and as  $p_2 < 0$ , roots  $\bar{\xi}_{0_3}$  and  $\bar{\xi}_{0_4}$  are imaginary. Finally, abscissa  $\bar{\xi}_0$  of the stress point  $(\bar{\xi}_0, 0)$  intersecting negative  $\bar{\xi}$  - axis is given as,

$$\bar{\xi}_0 = f_c \bar{\xi}_{0_1} \quad (\text{B4})$$

### B.2. Determining $\bar{\xi}_1(q(\kappa^p))$

The point  $(\bar{\xi}_1(q(\kappa^p)), 1)$  on the cap function  $F_c$  given by Eq. (21) is the transition point such that  $\forall \bar{\xi} \geq \bar{\xi}_1(q(\kappa^p))$ :  $F_c(\bar{\xi}, \bar{\xi}_1(q(\kappa^p))) = 1$ . In order to determine  $\bar{\xi}_1(q(\kappa^p))$ , we first determine the stress coordinate which is the maxima of the yield surface given by Eq. (23) ( $q(\kappa^p)$  is subsequently referred as  $q$  and, as  $\bar{\xi}_1(q(\kappa^p))$  as  $\bar{\xi}_1$ ). Let this point be referred as  $(\bar{\xi}_{max}, \bar{\rho}_{max})$ . Differentiating Eq. (23) and noting that  $\frac{d\bar{\rho}}{d\bar{\xi}}|_{(\bar{\xi}_{max}, \bar{\rho}_{max})} = 0$ , we obtain,

$$\begin{aligned} 2 \left[ (1-q) \left( \frac{\bar{\rho}_{max}}{\sqrt{6}f_c} + \frac{\bar{\xi}_{max}}{\sqrt{3}f_c} \right)^2 + \sqrt{\frac{3}{2}} \frac{\bar{\rho}_{max}}{f_c} \right] \\ \times \left[ 2(1-q) \left( \frac{\bar{\rho}_{max}}{\sqrt{6}f_c} + \frac{\bar{\xi}_{max}}{\sqrt{3}f_c} \right) \right] + m_0q^2 = 0 \quad (\text{B5}) \end{aligned}$$

let  $z = \frac{\bar{\rho}_{max}}{\sqrt{6}f_c} + \frac{\bar{\xi}_{max}}{\sqrt{3}f_c}$ , which implies

$$(1-q)z^3 + \left( \sqrt{\frac{3}{2}} \frac{\bar{\rho}_{max}}{f_c} \right) z + \frac{m_0q^2}{4(1-q)} = 0 \quad (\text{B6})$$

Eq. (B6) is a cubic equation in  $z$ . Next, we define the following variables

$$\Delta_0 = -3(1-q)\sqrt{\frac{3}{2}} \frac{\bar{\rho}_{max}}{f_c}; \quad \Delta_1 = \frac{27}{4}m_0q^2(1-q) \quad (\text{B7})$$

Note that  $\Delta_0 \leq 0$  and  $\Delta_1 \geq 0$ . As the discriminant of the equation (Eq. (B6)) is less than zero, it only has one real root denoted as  $z_0$  given by,

$$z_0 = -\frac{1}{3(1-q)} \left( P + \frac{\Delta_0}{P} \right) = \frac{\bar{\rho}_{max}}{\sqrt{6}f_c} + \frac{\bar{\xi}_{max}}{\sqrt{3}f_c} \quad (\text{B8})$$

where  $P = \sqrt[3]{\frac{\Delta_1 + \sqrt{\Delta_1^2 - 4\Delta_0^3}}{2}}$  is approximated as  $P = \sqrt[3]{\Delta_1}$  for simplification. We note that this simplification would result in the determination the stress point  $(\bar{\xi}_{max}, \bar{\rho}_{max})$  which is very close to the true maxima of the yield surface given by Eq. (23). From Eq. (B8), we obtain the following relation between  $\bar{\xi}_{max}$  and  $\bar{\rho}_{max}$ ,

$$\frac{\bar{\xi}_{max}}{f_c} = \frac{\bar{\rho}_{max}}{\sqrt{2}f_c} \left( \frac{3}{P} - 1 \right) - \frac{P}{\sqrt{3}(1-q)} \quad (\text{B9})$$

Substituting Eq. (B9) in the yield surface Eq. (23) we obtain a quartic equation in  $\frac{\bar{\rho}_{max}}{f_c}$  given as

$$A_1 \left( \frac{\bar{\rho}_{max}}{f_c} \right)^4 + B_1 \left( \frac{\bar{\rho}_{max}}{f_c} \right)^3 + C_1 \left( \frac{\bar{\rho}_{max}}{f_c} \right)^2 + D_1 \left( \frac{\bar{\rho}_{max}}{f_c} \right) + E_1 = 0$$

where,

$$A_1 = \frac{9(1-q)^2}{4P^4}; \quad B_1 = \sqrt{\frac{3}{2}} \frac{(1-q)}{P^2}; \quad C_1 = \frac{1}{2};$$

$$D_1 = \frac{1}{9} \sqrt{\frac{2}{3}} \frac{p^2}{(1-q)} + m_0 q^2 \left( \frac{\sqrt{3}}{p\sqrt{2}} - \frac{\Gamma(\cos \bar{\theta}, e) - 1}{\sqrt{3}} \right);$$

$$E_1 = \frac{p^4}{81(1-q)^2} - \frac{m_0 q^2 p}{3(1-q)} - q^2 \quad (B10)$$

To solve for  $\bar{\rho}_{max}$ , we further define the following variables,

$$r_1 = \frac{(8A_1 C_1 - 3B_1^2)}{8A_1^2}; \quad r_2 = \frac{(B_1^3 - 4A_1 B_1 C_1 + 8A_1^2 D_1)}{8A_1^3};$$

$$r_3 = C_1^2 - 3B_1 D_1 + 12A_1 E_1; \quad r_4 = 2C_1^3 - 9B_1 C_1 D_1 + 27A_1 D_1^2 + 27B_1^2 E_1 - 72A_1 C_1 E_1$$

$$s_1 = \left( \frac{(r_4 + \sqrt{r_4^2 - 4r_3^3})}{2} \right)^{\frac{1}{3}}; \quad s_2 = \frac{1}{2} \sqrt{-\frac{2}{3} r_1 + \frac{1}{3A_1} \left( s_1 + \frac{r_3}{s_1} \right)}$$

(B11)

Finally,  $\bar{\rho}_{max}$  is given as,

$$\bar{\rho}_{max} = f_c \left[ -\frac{B_1}{4A_1} - s_2 + \frac{1}{2} \sqrt{-4s_2^2 - 2r_1 + \frac{r_2}{s_2}} \right] \quad (B12)$$

We note that the transition point on the cap function  $F_c$  is given as  $(\bar{\xi}_1(q(\kappa^p)), 1)$ , and corresponding transition point on the yield function  $F$  is  $(\bar{\xi}_1(q(\kappa^p)), \bar{\rho}_1(q(\kappa^p)))$ . The ordinate  $\bar{\rho}_1(q(\kappa^p))$  of the transition point on the yield surface  $F$ , is considered to be less than  $\bar{\rho}_{max}$  and is given as,

$$\bar{\rho}_1 = \alpha \bar{\rho}_{max}; \quad 0 < \alpha < 1 \quad (B13)$$

In this work, we considered  $\alpha = \frac{2}{3\Gamma(\cos \bar{\theta}, e)}$ . Once  $\bar{\rho}_1$  is known, the abscissa  $\bar{\xi}_1$  can be determined from the parabolic function for the loading surface  $F_L$  (Eq. (16)) as follows

$$\bar{\xi}_1 = \frac{\sqrt{3}}{m_0 q^2} \left( f_c q^2 - \frac{m_0 q^2 \Gamma(\cos \bar{\theta}, e)}{\sqrt{6}} \bar{\rho}_1 - \frac{3}{2f_c} \bar{\rho}_1^2 \right) \quad (B14)$$

### Appendix C. Gradient of F and F<sup>p</sup>

The first derivatives of  $\bar{\xi}$ ,  $\bar{\rho}$  and  $\bar{\theta}$  with respect to the stress tensor  $\bar{\sigma}_{ij}$  are determined first which are used subsequently to evaluate the gradient of yield function  $F$  and plastic potential  $F^p$ . Using Eq. (15), we obtain the following,

$$\frac{\partial \bar{\xi}}{\partial \bar{\sigma}_{ij}} = \frac{1}{\sqrt{3}} \frac{\partial \bar{I}_1}{\partial \bar{\sigma}_{ij}}; \quad \frac{\partial \bar{\rho}}{\partial \bar{\sigma}_{ij}} = \frac{1}{\rho} \frac{\partial \bar{J}_2}{\partial \bar{\sigma}_{ij}}; \quad \frac{\partial \bar{\theta}}{\partial \bar{\sigma}_{ij}} = \frac{\partial \bar{\theta}}{\partial \bar{J}_2} \frac{\partial \bar{J}_2}{\partial \bar{\sigma}_{ij}} + \frac{\partial \bar{\theta}}{\partial \bar{J}_3} \frac{\partial \bar{J}_3}{\partial \bar{\sigma}_{ij}} \quad (C1)$$

where,

$$\frac{\partial \bar{\theta}}{\partial \bar{J}_2} = \frac{3\sqrt{3}}{4 \sin(3\bar{\theta})} \frac{\bar{J}_3}{\sqrt{\bar{J}_2}}; \quad \frac{\partial \bar{\theta}}{\partial \bar{J}_3} = -\frac{\sqrt{3}}{2 \sin(3\bar{\theta})} \frac{1}{\sqrt{\bar{J}_2}} \quad (C2)$$

and,

$$\frac{\partial \bar{I}_1}{\partial \bar{\sigma}_{ij}} = \delta_{ij}; \quad \frac{\partial \bar{J}_2}{\partial \bar{\sigma}_{ij}} = \bar{s}_{ij} = \bar{\sigma}_{ij} - \frac{\bar{I}_1}{3} \delta_{ij}; \quad \frac{\partial \bar{J}_3}{\partial \bar{\sigma}_{ij}} = \bar{s}_{ik} \bar{s}_{kj} - \frac{2}{3} \bar{J}_2 \delta_{ij} \quad (C3)$$

Next, gradient of  $F$  and  $F^p$  are given as follows,

$$\frac{\partial F}{\partial \bar{\sigma}_{ij}} = n_{ij} = \frac{\partial F}{\partial \bar{\xi}} \frac{\partial \bar{\xi}}{\partial \bar{\sigma}_{ij}} + \frac{\partial F}{\partial \bar{\rho}} \frac{\partial \bar{\rho}}{\partial \bar{\sigma}_{ij}} + \frac{\partial F}{\partial \bar{\theta}} \frac{\partial \bar{\theta}}{\partial \bar{\sigma}_{ij}}$$

$$\frac{\partial F^p}{\partial \bar{\sigma}_{ij}} = m_{ij} = \frac{\partial F^p}{\partial \bar{\xi}} \frac{\partial \bar{\xi}}{\partial \bar{\sigma}_{ij}} + \frac{\partial F^p}{\partial \bar{\rho}} \frac{\partial \bar{\rho}}{\partial \bar{\sigma}_{ij}} + \frac{\partial F^p}{\partial \bar{\theta}} \frac{\partial \bar{\theta}}{\partial \bar{\sigma}_{ij}} \quad (C4)$$

The derivatives of  $\bar{\xi}$ ,  $\bar{\rho}$  and  $\bar{\theta}$  with respect to the stress tensor  $\bar{\sigma}_{ij}$  used in Eq. (B4) are determined from Eqs. (C1)–(C3); using

Eqs. (21), (22), (32) and (33), derivatives of  $F$  and  $F^p$  with respect to these stress invariants are evaluated as follows,

$$\frac{\partial F}{\partial \bar{\xi}} = q^2(\kappa^p) \left[ \left\{ m_0 \Gamma(\cos \bar{\theta}, e) \frac{\bar{\rho}}{\sqrt{6} f_c} + 2F_c \left( m_0 \frac{\bar{\xi}}{\sqrt{3} f_c} - 1 \right) \right\} \frac{\partial F_c}{\partial \bar{\xi}} + m_0 \frac{\bar{\xi}}{\sqrt{3} f_c} F_c^2 \right] \quad (C5)$$

$$\frac{\partial F^p}{\partial \bar{\xi}} = \frac{\partial F}{\partial \bar{\xi}} + \frac{q^2(\kappa^p)}{f_c} \left[ A_f \exp \frac{R_f(\bar{\xi})}{B_f} + C_f \right] \quad (C6)$$

where parameters  $A_f$ ,  $B_f$  and  $C_f$ , and function  $R_f(\bar{\xi})$  are described in Eq. (32) and (33).  $\frac{\partial F_c}{\partial \bar{\xi}}$  is given as follows,

$$\frac{\partial F_c}{\partial \bar{\xi}} = -\frac{1}{F_c} \left[ \frac{\bar{\xi} - \bar{\xi}_1(q(\kappa^p))}{(\bar{\xi}_0(q(\kappa^p)) - \bar{\xi}_1(q(\kappa^p)))^2} \right] H(\bar{\xi}_1(q(\kappa^p)) - \bar{\xi}) \quad (C7)$$

where  $H(x_1 - x)$  is a Heaviside step function such that  $H(x_1 - x) = 1$  for  $x_1 > x$  and  $= 0$  otherwise.

Next, derivatives of  $F$  and  $F^p$  with respect to  $\bar{\rho}$  and  $\bar{\theta}$  are given as follows,

$$\frac{\partial F}{\partial \bar{\rho}} = \frac{\partial F^p}{\partial \bar{\rho}} = 3 \frac{\bar{\rho}}{f_c^2} + \frac{m_0 q^2(\kappa^p) \Gamma(\cos \bar{\theta}, e)}{\sqrt{6} f_c} F_c \quad (C8)$$

$$\frac{\partial F}{\partial \bar{\theta}} = \frac{\partial F^p}{\partial \bar{\theta}} = m_0 q^2(\kappa^p) \frac{\bar{\rho}}{\sqrt{6} f_c} F_c \frac{\partial \Gamma(\cos \bar{\theta}, e)}{\partial \bar{\theta}}$$

where,

$$\frac{\partial \Gamma(\cos \bar{\theta}, e)}{\partial \bar{\theta}} = \frac{1}{2(1-e^2) \cos \bar{\theta} + (2e-1) \sqrt{4(1-e^2) \cos^2 \bar{\theta} + 5e^2 - 4e}}$$

$$\left( -8(1-e^2) \cos \bar{\theta} \sin \bar{\theta} + (4(1-e^2) \cos^2 \bar{\theta} + (2e-1)^2) \right.$$

$$\left. \left( 2(1-e^2) \sin \bar{\theta} + \frac{4(2e-1)(1-e^2) \cos \bar{\theta} \sin \bar{\theta}}{\sqrt{4(1-e^2) \cos^2 \bar{\theta} + 5e^2 - 4e}} \right) \right) \quad (C9)$$

### References

- Ashby, M.F., Sammis, C.G., 1990. The damage mechanics of brittle solids in compression. *Pure Appl. Geophys.* 133, 489–521.
- Bazant, Z., Xiang, Y., Adley, M., Prat, P., Akers, S., 1996b. Microplane model for concrete. II: data delocalization and verification. *J. Eng. Mech.* 122, 255–262.
- Bazant, Z.P., 1986. Mechanics of distributed cracking. *Applied. Mech. Rev.* 39, 675–705.
- Bazant, Z.P., Bishop, F.C., Chang, T.P., 1986. Confined compression tests of cement paste and concrete up to 300 Ksi. *ACI J.* 33, 553–560.
- Bazant, Z.P., Oh, B.H., 1983. Crack band theory for fracture of concrete. *Mater. Struct.* 16, 155–177.
- Bazant, Z.P., Pijaudier-Cabot, G., 1989. Measurement of characteristic length of non-local continuum. *J. Eng. Mech.* 115, 755–767.
- Bhat, H.S., Rosakis, A.J., Sammis, C.G., 2012. A micromechanics based constitutive model for brittle failure at high strain rates. *J. Appl. Mech.* 79 (031016), 031011–031012.
- Burlion, N., Pijaudier-Cabot, G., Dahan, N., 2001. Experimental analysis of compaction of concrete and mortar. *Int. J. Numer. Anal. Methods Geomech.* 25, 1467–1486.
- Caner, F.C., Bazant, Z.P., 2013. Microplane model M7 for plain concrete. I: formulation. *J. Eng. Mech.* 139, 1714–1723.
- Caner, F.C., Bazant, Z.P., 2000. Microplane model M4 for concrete. II. Algorithm and calibration. *J. Eng. Mech.* 126, 954–961.
- Cervenka, J., Papanikolaou, V.K., 2008. Three dimensional combined fracture–plastic material model for concrete. *Int. J. Plast.* 24, 2192–2220.
- Cicekli, U., Voyiadjis, G.Z., Al-Rub, R.K.A., 2007. A plasticity and anisotropic damage model for plain concrete. *Int. J. Plast.* 23, 1874–1900.
- Deshpande, V.S., Evans, A.G., 2008. Inelastic deformation and energy dissipation in ceramics: a mechanism-based constitutive model. *J. Mech. Phys. Solids* 56, 3077–3100.

- Etse, G., Willam, K., 1994. Fracture energy formulation for inelastic behavior of plain concrete. *J. Eng. Mech.* 120, 1983–2011.
- Folino, P., Etse, G., 2012. Performance dependent model for normal and high strength concretes. *Int. J. Solids Struct.* 49, 701–719.
- Garrison, W.M., Moody, N.R., 1987. Ductile fracture. *J. Phys. Chem. Solids* 48, 1035–1074.
- Gopalaratnam, V.S., Shah, S.P., 1985. Softening response of plain concrete in direct tension. *J. Am. Concr. Inst.* 82, 310–323.
- Grassl, P., Jirásek, M., 2006. Damage-plastic model for concrete failure. *Int. J. Solids Struct.* 43, 7166–7196.
- Grassl, P., Lundgren, K., Gylltoft, K., 2002. Concrete in compression: a plasticity theory with a novel hardening law. *Int. J. Solids Struct.* 39, 5205–5223.
- Grassl, P., Xenos, D., Nyström, U., Rempling, R., Gylltoft, K., 2013. CDPM2: a damage-plasticity approach to modelling the failure of concrete. *Int. J. Solids Struct.* 50, 3805–3816.
- Green, S.J., Swanson, S.R., 1973. Static Constitutive Relations for Concrete. Air Force Weapons Laboratory, Kirtland Air Force Base.
- Han, D.J., Chen, W.F., 1987. Constitutive modeling in analysis of concrete structures. *J. Eng. Mech.* 113, 577–593.
- Horii, H., Nemat-Nasser, S., 1986. Brittle failure in compression: splitting, faulting, and brittle-ductile transition. *Philos. Trans. R. Soc. London A* 319, 337–374.
- Horstemeyer, M.F., Lathrop, J., Gokhale, A.M., Dighe, M., 2000. Modeling stress state dependent damage evolution in a cast Al-Si-Mg aluminum alloy. *Theor. Appl. Fract. Mech.* 33, 31–47.
- Imran, I., Pantazopoulou, S.J., 1996. Experimental study of plain concrete under triaxial stress. *ACI Struct. J.* 93, 589–601.
- Jirásek, M., Bažant, Z.P., 2002. *Inelastic Analysis of Structures*. John Wiley and Sons, Chichester, p. 365.
- Ju, J.W., 1990. Isotropic and anisotropic damage variables in continuum damage mechanics. *J. Eng. Mech.* 116, 2764–2770.
- Kachanov, M.L., 1982. A microcrack model of rock inelasticity Part I: Frictional sliding of microcracks. *Mech. Mater.* 1, 19–27.
- Karsan, I.D., Jirsa, J.O., 1969. Behavior of concrete under compressive loadings. *J. Struct. Div. ASCE* 95, 2543–2563.
- Kupfer, H., Hilsdorf, H.K., Rušch, H., 1969. Behavior of concrete under biaxial stresses. *J. Am. Concr. Inst.* 66, 656–666.
- Lämmer, H., Tsakmakis, C., 2000. Discussion of coupled elastoplasticity and damage constitutive equations for small and finite deformations. *Int. J. Plast.* 16, 495–523.
- Lee, J., Fenves, G.L., 1998. Plastic damage model for cyclic loading of concrete structures. *J. Eng. Mech.* 124, 892–900.
- Lemaitre, J., 1985a. Coupled elasto-plasticity and damage constitutive equations. *Comput. Methods Appl. Mech. Eng.* 51, 31–49.
- Lemaitre, J., Chaboche, J.L., 1998. *Mechanics of Solid Materials*.
- Lu, X., Tzu, C., Hsu, T., 2007. Stress-strain relations of high-strength concrete under triaxial compression. *J. Mater. Civil Eng.* 19, 261–268.
- Lubliner, J., Oliver, J., Oller, S., Onate, E., 1989. A plastic-damage model for concrete. *Int. J. Solids Struct.* 25, 299–326.
- Luccioni, B., Oller, S., Danesi, R., 1996. Coupled plastic-damaged model. *Comput. Methods Appl. Mech. Eng.* 129, 81–89.
- Menétrey, P., Walther, R., Zimmermann, T., Willam, K.J., Regan, P.E., 1997. Simulation of punching failure in reinforced-concrete structures. *J. Struct. Eng.* 123, 652–659.
- Menétrey, P., Willam, K.J., 1995. Triaxial failure criterion for concrete and its generalization. *ACI Struct. J.* 92, 311–318.
- Menzela, A., Ekh, M., Runesson, K., Steinmann, P., 2005. A framework for multiplicative elastoplasticity with kinematic hardening coupled to anisotropic damage. *Int. J. Plast.* 21, 397–434.
- Oliver, J., 1989. A consistent characteristic length for smeared cracking model. *Int. J. Numer. Methods Eng.* 28, 461–474.
- Paliwal, B., Ramesh, K.T., 2008. An interacting micro-crack damage model for failure of brittle materials under compression. *J. Mech. Phys. Solids* 56, 896–923.
- Papanikolaou, V.K., Kappos, A.J., 2007. Confinement-sensitive plasticity constitutive model for concrete in triaxial compression. *Int. J. Solids Struct.* 44, 7021–7048.
- Pijaudier-Cabot, G., Bažant, Z.P., 1987. Nonlocal damage theory. *J. Eng. Mech.* 113, 1512–1533.
- Poinard, C., Malecot, Y., Daudeville, L., 2010. Damage of concrete in a very high stress state: experimental investigation. *Mater. Struct.* 43, 15–29.
- Pramono, E., Willam, K., 1989. Fracture energy-based plasticity formulation of plain concrete. *J. Eng. Mech.* 115, 1183–1204.
- Salari, M.R., Saeb, S., Willam, K.J., Patchet, S.J., Carrasco, R.C., 2004. A coupled elasto-plastic damage model for geomaterials. *Comput. Methods Appl. Mech. Eng.* 193, 2625–2643.
- Sánchez, P.J., Huespe, A.E., Oliver, J., Diaz, G., Sonzogni, V.E., 2011. A macroscopic damage-plastic constitutive law for modeling quasi-brittle fracture and ductile behavior of concrete. *Int. J. Numer. Anal. Methods Geomech.* 36, 546–573.
- Sfer, D., Carol, I., Gettu, R., Etse, G., 2002. Study of the behavior of concrete under triaxial compression. *J. Eng. Mech.* 128, 156–163.
- Smith, S., Willam, K., Gerstle, K., S., S., 1989. Concrete over the top, or is there life after peak. *ACI Mater. J.* 86, 491–497.
- Tapponnier, P., Brace, W.F., 1976. Development of stress-induced microcracks in Westerly granite. *Int. J. Rock Mech. Min. Sci.* 13, 103–112.
- Voyiadjis, G.Z., Taqieddin, Z.N., Kattan, P.I., 2008. Anisotropic damage-plasticity model for concrete. *Int. J. Plast.* 24, 1946–1965.
- Willam, K.J., Warnke, E.P., 1975. Constitutive model for the triaxial behavior of concrete. In: *ISMES Seminar on Concrete Structures Subjected to Triaxial Stresses*. Bergamo, Italy, pp. 1–30.
- Wu, J.Y., Li, J., Faria, R., 2006. An energy release rate-based plastic-damage model for concrete. *Int. J. Solids Struct.* 43, 583–612.
- Voyiadjis, G.Z., Taqieddin, Z.N., 2009. Elastic plastic and damage model for concrete materials: Part I - theoretical formulation. *Int. J. Struct. Changes Solids* 1, 31–59.